Role of Synchronization in Magnetless Nonreciprocal Devices Based on Commutated Transmission Lines

Zhicheng Xiao,[1,†] Dimitrios L. Sounas,[1,2,†] Aravind Nagulu,[3,†] Mykhailo Tymchenko,[1] Tolga Dinc,[3] Harish Krishnaswamy,[3] and Andrea Alù[1,4,*]

[1] *Department of Electrical and Computer Engineering, The University of Texas at Austin, Austin, Texas 78712, USA*

[2] *Department of Electrical and Computer Engineering, Wayne State University, Detroit, Michigan 48202, USA*

[3] *Department of Electrical Engineering, Columbia University, New York, New York 10027, USA*

[4] *Advanced Science Research Center, City University of New York, New York, New York 10031, USA*

(Received 27 June 2019; revised manuscript received 2 April 2020; accepted 11 May 2020; published 15 June 2020)

Commutated transmission lines have been recently explored as an interesting way to break Lorentz reciprocity, avoiding any resonant structure, and enabling broad bandwidths with giant isolation combined with lenient requirements on the modulation frequency. The scheme relies on precise synchronization among different switches connected through transmission lines, offering in principle infinite bandwidth. Here, we investigate the effects of realistic switching parameters and synchronization on the device performance, providing interesting physical insights on the operation of these devices. Our research shows that the nonreciprocal response of these systems experiences a linear regression of insertion loss and isolation with respect to the timing error among switches. Remarkably, impedance matching and nonreciprocal phase shifts are immune from synchronization issues, and reasonable levels of synchronization errors still guarantee low insertion loss and good isolation. Our study also provides practical guidelines to envision nonreciprocal devices based on commutated modulation of conductivity, opening interesting opportunities for several fields of technology, including wireless communications, quantum technologies, and photonic circuits.

DOI: 10.1103/PhysRevApplied.13.064033

I. INTRODUCTION

Time-reversal symmetry (TRS) is a fundamental property of many classical physical systems [1–4], which dictates that a system remains symmetric under the time-reversal operation $\mathscr{T}: t \rightarrow -t$. In linear time-invariant (LTI) and nongyrotropic electromagnetic systems, TRS leads to the well-known Lorentz reciprocity theorem [5]. Breaking Lorentz reciprocity allows creating asymmetric transmission when exciting from different directions, and it has been an exciting research topic over the past decade [6–21], since it shows great promise for devices and applications, such as on-chip optical diodes [6,16], [17], superconducting quantum circuits [18], and circulators for full-duplex communication systems [19–26].

The conventional approach to break Lorentz reciprocity is to bias a system with a quantity that is odd-symmetric under time-reversal operation, such as linear velocity **v**, conduction current **J**, or magnetic field **B**. Among all these approaches, magnetic bias is by far the most common for microwave and optical nonreciprocal devices. However, devices based on this approach tend to be bulky, expensive, and incompatible with chip-scale fabrication processes, due to lattice mismatch between magnetic nonreciprocal media and semiconductors. Nonlinear Kerr effects in asymmetric resonant structures provide solutions to several of these problems, including bias-free nonreciprocity, small form factor, and compatibility with integrated systems technology [17,24]. Unfortunately, however, nonlinear nonreciprocity is characterized by fundamental limitations, such as narrow dynamic range, intensity-dependent operation, sensitivity to noise, a trade-off between insertion loss and transmission, and operation for nonsimultaneous excitation from different ports [27–29]. Another approach that has proven very attractive for the design of magnetless nonreciprocal devices without the problems of nonlinear systems is based on time modulation of permittivity. Different types of such linear time-variant (LTV) systems have been proposed so far, including systems with traveling wave modulation [6,7], effective gauge fields [8,30], and angular-momentum biasing [11,12,19], which have proven to be dynamic and versatile platforms for many nonreciprocal devices. For example, Ref. [31]

*aalu@gc.cuny.edu

†These authors contribute equally to this paper.

presented experimental results for a rf circulator using angular-momentum biasing induced by an orchestrated modulation of varactors. The insertion loss of the circulator was smaller than 2 dB and the isolation was larger than 20 dB at 1 GHz, which are close to the metrics required in practical full-duplex radios.

A related approach to realize nonreciprocal devices is based on transmission-line commutation. Such LTV devices leverage the fact that conductivity can be modulated with a large contrast, exceeding 10^5 between *on* and *off* states at frequencies up to tens of GHz. Such a modulation can be typically achieved using transistors as switches, making it particularly attractive to realize miniaturized and fully integrable nonreciprocal devices. Synchronized conductivity modulation has been employed to realize isolators and gyrators with theoretically infinite bandwidth, as well as a circulator fully integrated in a 65-nm CMOS chip [13]. Synchronized conductivity modulation across transmission lines has enabled high-performance circulators, making these approaches viable for commercial applications [32]. Specifically, transmission-line commutation has enabled CMOS-integrated circulators in the millimeter-wave frequency range (25-GHz operation in Ref. [20] and 60-GHz operation in Ref. [33]) as well as circulators with insertion losses of around 2 dB, isolation greater than 40 dB, and watt-level power handling at radio frequencies [32]. Conductivity modulation is preferable over temporal modulation of the real part of permittivity, since the latter is a weak effect, as well as over capacitance modulation in varactors, whose nonlinearity makes them not ideal for high-power applications [6,7,11,12,19]. Nevertheless, the performance of these devices relies heavily on synchronization of the clocking signals.

In this paper, we explore the effects of realistic switch desynchronization on the performance of this class of nonreciprocal devices, analyzing to what degree this effect may degrade the device performance. We quantitatively evaluate the impact of timing errors on various key metrics, focusing on three types of nonreciprocal devices originally introduced in Ref. [20,34]: a gyrator, an isolator, and a circulator, which respectively exhibit nonreciprocal phase response, nonreciprocal amplitude response, and unidirectional flow of signals. In Secs. II–IV, we present ideal singly balanced nonreciprocal designs and explain how commutated switches can be employed to create nonreciprocal phase or amplitude responses. Then, we study realistic scenarios in which synchronization issues arise. Our study indicates that the network is still perfectly matched in the presence of a switch timing error $\Delta\tau$. However, the transmission and insertion loss experience a linear recession versus $\Delta\tau$. A differential configuration is then analyzed, with ideally infinite bandwidth. Compared with singly balanced configurations, differential geometries offer the additional advantage that the insertion loss is independent of the input signal frequency in the presence of timing errors. Finally, in Sec. V, we provide a case study for a realistic implementation of these circuits, and we conclude the paper by discussing practical implementation guidelines for the considered devices and provide an outlook on these results and their implications on technology.

II. GYRATORS

A gyrator is a nonreciprocal phase shifter offering 180° phase-shift difference when excited from opposite directions [35,36]. Tellegen showed that a combination of gyrators and other reciprocal lumped elements can implement any linear operation of interest [35]. In this section, we review how commutated transmission lines can be employed to create a nonreciprocal phase response, and introduce singly balanced and differential gyrator designs, studying the effect of synchronization issues. Our calculations and modeling are based on time- and frequency-domain analyses, further validated numerically using the homemade Floquet scattering matrix (FSM) approach [37] and commercial Advanced Design System (ADS) software.

A. Singly balanced gyrator

A schematic of a singly balanced nonreciprocal phase shifter is shown in Fig. 1(a). A lossless transmission-line segment is sandwiched between two switches, with switching signals $P_1(t)$ and $P_2(t)$ shown in Fig 1(c), where "1" and "0" represent "infinite" and "zero" conductivity (full and zero transmission), respectively. The second switch P_2 is delayed by a quarter period of the modulation signal compared to the first switch P_1. The transmission-line

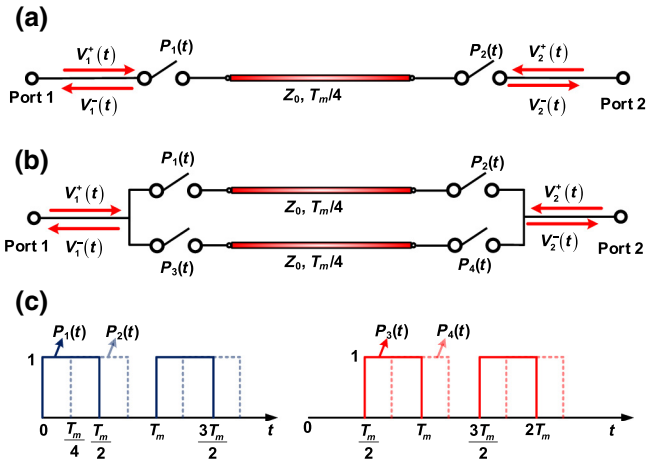

FIG. 1. Circuit schematic and modulation signals of the gyrator. (a) Circuit schematic of a single-branch gyrator. (b) Circuit schematic of a singly balanced gyrator. (c) Modulation signals. "1" stands for "*on*", and "0" stands for "*off* ".

delay is also chosen to be equal to a quarter period of the modulation signal, and assuming nondispersive propagation. When we apply an excitation at port 1 and switch 1 is *on*, the signal passes through the transmission line and switch 2, traveling to port 2. If the switch 1 is *off*, the input signal is totally reflected at port 1. On the other hand, a signal incident at port 2 when switch 2 is closed, after propagation through the delay line, finds switch 1 in its open state and is reflected towards port 2. Upon reaching this port, switch 2 is also open and the signal experiences another reflection towards port 1, where it eventually is transmitted after traveling along the transmission line three times. If switch 2 is open, the incident signal at port 2 is totally reflected. The temporal responses of the output signals at the two ports are hence described by

$$V_2^-(t) = V_1^+\left(t - \frac{T_m}{4}\right) P_1\left(t - \frac{T_m}{4}\right), \tag{1}$$

$$V_1^-(t) = V_1^+(t)[1 - P_1(t)], \tag{2}$$

$$V_1^-(t) = V_2^+\left(t - \frac{3T_m}{4}\right) P_2\left(t - \frac{3T_m}{4}\right), \tag{3}$$

$$V_2^-(t) = V_2^+(t)[1 - P_2(t)], \tag{4}$$

where T_m is the modulation period, $V_i^+(t)$ is the input signal at ith port, and $V_i^-(t)$ is the output signal at ith port. Equations (1)–(2) and (3)–(4) apply for excitation from ports 1 and 2, respectively.

As we see from Eqs. (1)–(4), the time delay of forward and backward transmitted signals is nonreciprocal, and equal to $T_m/4$ and $3T_m/4$, respectively, which results in a direction-dependent phase. This is reflected in the frequency response of the system, which is rigorously derived in Appendix A. The system generates multiple frequencies, due to its time-varying nature, but, by looking at the zeroth Fourier harmonic, we readily obtain the nonreciprocal scattering matrix of the fundamental tone:

$$S(\omega) = \frac{1}{2}\begin{bmatrix} 1 & e^{-j\omega\frac{3T_m}{4}} \\ e^{-j\omega\frac{T_m}{4}} & 1 \end{bmatrix}, \tag{5}$$

which is consistent with the time-domain description above. Equation (5) clearly shows a nonreciprocal phase response for forward and backward transmitted signals. When the input frequency satisfies the condition $\omega = (2k+1)\omega_m$, where $k = 0, 1, 2\ldots$, the phase difference between forward and backward transmitted signals becomes π and the device operates as a lossy gyrator.

From the frequency-domain standpoint, each switch acts as a frequency mixer, which converts the incoming signal from either of the two ports into an infinite discrete series of harmonics with certain phases. Each of these harmonics propagate along the transmission line and, upon reaching the second switch, the signal experiences another mixing event, which partially converts these harmonics to the fundamental tone, leading to an overall 6-dB insertion loss [factor 1/2 in Eq. (5)]. During the mixing events, the signals pick up modulation phases with positive and negative sign at the first and second switch, respectively. As a result, the output signal acquires an additional phase equal to the phase difference between switches. Since the two switches are closed with a delay $T_m/4$ and $3T_m/4$ with respect to each other in the forward and backward directions respectively, the phase of the output signal is different in opposite directions, as observed in Eq. (5).

The 6-dB insertion loss of the single-branch gyrator described in Eq. (5) can be compensated by adding a second branch with complementary clocks, as shown in Fig. 1(b). In this case, the output signal is the superposition of the transmitted signal through the top branch, given by Eqs. (1)–(4), and the one through the bottom branch, which can be derived by applying a $T_m/2$ delay to all switches. Then, it is easy to find that the total output signals at the ports are given by

$$\begin{cases} V_2^-(t) = V_1^+(t - T_m/4), \\ V_1^-(t) = 0, \end{cases} \tag{6}$$

for excitation from port 1 and

$$\begin{cases} V_1^-(t) = V_2^+\left(t - \frac{3T_m}{4}\right), \\ V_2^-(t) = 0, \end{cases} \tag{7}$$

for excitation from port 2. By converting Eqs. (6) and (7) to frequency domain, we find that the scattering matrix for the fundamental tone is

$$S(\omega) = \begin{bmatrix} 0 & e^{-j\omega\frac{3T_m}{4}} \\ e^{-j\omega\frac{T_m}{4}} & 0 \end{bmatrix}. \tag{8}$$

A π nonreciprocal phase shift occurs at $\omega = (2k+1)\omega_m$, where $k = 0, 1, 2, 3, \ldots$, at which the device operates as an ideal, infinite bandwidth, lossless gyrator. Figures 2(b) and 2(c) show the amplitude and phase characteristics of the forward and backward transmission coefficients S_{21} and S_{12}, respectively. Indeed, the amplitude of transmission coefficient is unitary and frequency independent, while the

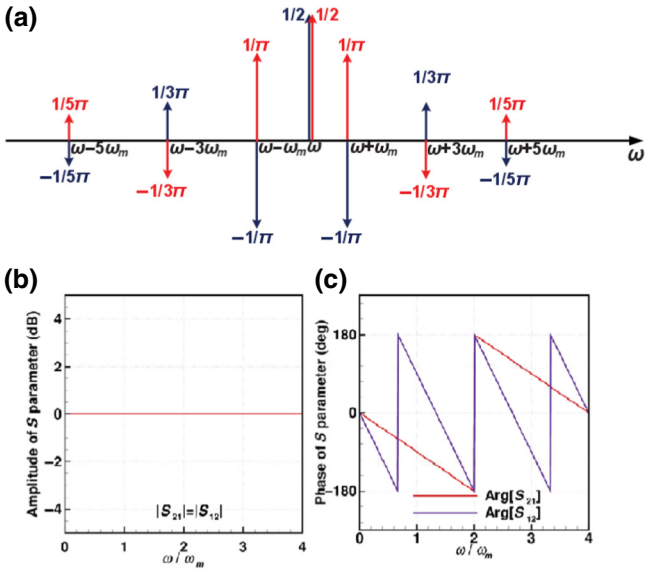

FIG. 2. Harmonics of forward transmitted signal and S parameters of the singly balanced gyrator. (a) Harmonics of forward transmitted signal. The blue line marks the harmonics of the first branch with switches P1 and P2. The red line stands for the harmonics of the complementary branch with switches P3 and P4. (b) Magnitude of S parameters of a singly balanced gyrator. (c) Phase of S parameters of a singly balanced gyrator.

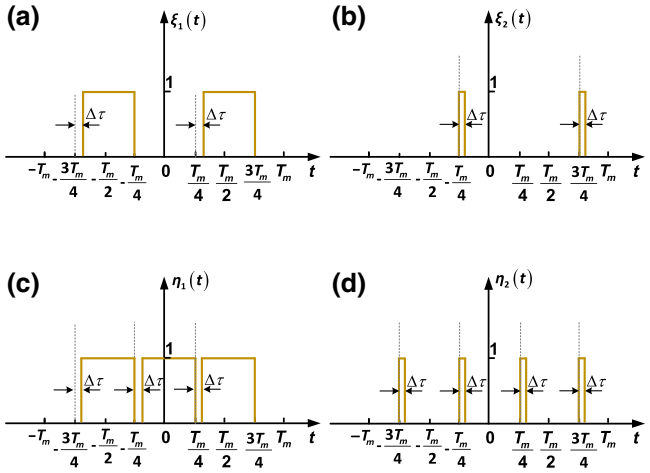

FIG. 3. Envelope of modulated signals of the gyrator with timing error. (a) Forward transmitted signal envelope from excitation at port 1 of a single-branch gyrator with time delay $T_m/4$; (b) forward transmitted signal envelope from excitation at port 1 of a single-branch gyrator with time delay $3T_m/4$; (c) forward transmitted signal envelope from excitation at port 1 of a singly balanced gyrator with time delay $3T_m/4$; (d) forward transmitted signal envelope from excitation at port 1 of a singly balanced gyrator with time delay $T_m/4$.

π nonreciprocal phase shift occurs at discrete frequency points. The suppression of insertion loss in this system can also be understood by looking at the spectrum of the output signal from the two branches, presented in Fig. 2(a) (blue and red for the top and bottom branches, respectively). We can see that higher-order harmonics experience opposite phase shift in the two branches, leading to destructive interference at the output ports. On the other hand, the fundamental tone maintains the same phase shift in both branches, leading to constructive superposition at the output port. In other words, while each transmission-line arm sustains propagation of many harmonics, essentially the sampling of the input signal splits into two parallel lines, at the two ports the synchronization of the switches allows recombination of the signal, without any distortion. The overall transfer function operates as a pseudo-linear-time-invariant system [38], in which no frequency conversion occurs. It is obvious that this ideal response is not possible in the absence of ideal synchronization, hence it is important to consider the effect of imperfections in the switching network on the overall Floquet transfer matrix of the system.

In this context, consider the single-branch-gyrator design in Fig. 1(a) and assume now that the second switch has a small timing error $\Delta\tau$ with respect to the first one, $P_2(t) = P_1(t - T_m/4 - \Delta\tau)$. For a monochromatic excitation $e^{j\omega t}$ at port 1, most of the signal, overlapping with the waveform in Fig. 3(a), passes through the second switch with a time delay $T_m/4$, while a small tail, overlapping with the waveform in Fig. 3(b), bounces twice inside the transmission line and transmits through the second switch with time delay $3T_m/4$. The reflected signal $V_1^-(t)$ is not affected by the timing error. For monochromatic excitation $e^{j\omega t}$ at port 2, most of the signal, overlapping with the waveform in Fig. 3(a), passes through the first switch with delay $3T_m/4$, while a small tail overlapping with the waveform in Fig. 3(b), is transmitted through the transmission line with delay $T_m/4$. The time-domain response of this slightly desynchronized gyrator is described by

$$V_2^-(t) = V_1^+\left(t - \frac{T_m}{4}\right)\xi_1(t) + V_1^+\left(t - \frac{3T_m}{4}\right)\xi_2(t), \quad (9)$$

$$V_1^-(t) = V_1^+(t)[1 - P_1(t)], \quad (10)$$

$$V_1^-(t) = V_2^+\left(t - \frac{3T_m}{4}\right)\xi_1\left(t - \frac{3T_m}{4}\right) + V_2^+\left(t - \frac{T_m}{4}\right)\xi_2\left(t - \frac{T_m}{4}\right), \quad (11)$$

$$V_2^-(t) = V_2^+(t)[1 - P_2(t)], \quad (12)$$

where Eqs. (9)–(10) and (11)–(12) correspond to excitation from port 1 and port 2, respectively. The functions $\xi_1(t)$, $\xi_2(t)$ are envelopes of modulated signals and have a period T_m [see Figs. 3(a) and 3(b)]. The scattering matrix for the fundamental frequency component is readily obtained (see Appendix A):

$$S = \begin{bmatrix} \frac{1}{2} & \frac{|\Delta\tau|}{T_m} e^{-j\omega\frac{T_m}{4}} + \left(\frac{1}{2} - \frac{|\Delta\tau|}{T_m}\right) e^{-j\omega\frac{3T_m}{4}} \\ \left(\frac{1}{2} - \frac{|\Delta\tau|}{T_m}\right) e^{-j\omega\frac{T_m}{4}} + \frac{|\Delta\tau|}{T_m} e^{-j\omega\frac{3T_m}{4}} & \frac{1}{2} \end{bmatrix}, \tag{13}$$

which indicates that, at the operational frequency $\omega = (2k+1)\omega_m$, $k = 0, 1, 2, 3 \ldots$, the single-branch gyrator exhibits additional insertion loss of $2|\Delta\tau|/T_m$, proportional to the timing error.

Next, we study the balanced gyrator with timing error, and assume that the same timing error as between switches P_1 and P_2 is also applied to switches P_3 and P_4, i.e., $P_4(t) = P_3(t - T_m/4 - \Delta\tau)$. This assumption is practically reasonable because we can use single-pole-double-throw switches to replace P_1 and P_3, and P_2 and P_4. The temporal responses are then given by

$$V_2^-(t) = V_1^+\left(t - \frac{T_m}{4}\right)\eta_1(t) + V_1^+\left(t - \frac{3T_m}{4}\right)\eta_2(t), \tag{14}$$

$$V_1^-(t) = 0, \tag{15}$$

$$V_1^-(t) = V_2^+\left(t - \frac{3T_m}{4}\right)\eta_1\left(t - \frac{3T_m}{4}\right) + V_2^+\left(t - \frac{T_m}{4}\right)\eta_2\left(t - \frac{T_m}{4}\right), \tag{16}$$

$$V_2^-(t) = 0. \tag{17}$$

Again, here Eqs. (14)–(15) and (16)–(17) correspond to excitation from ports 1 and 2, respectively. $\eta_1(t)$, $\eta_2(t)$ are envelopes of modulated signals [see Figs. 3(c) and 3(d)]. Remarkably, despite the synchronization error, the network remains ideally matched at both ports. This result stems from the fact that the desynchronized tail transmits through the two-port network rather than bouncing back to the source. Harmonic analysis of this singly balanced gyrator with timing error is given in Appendix A.

Figure 4 shows the amplitude of harmonics of a singly balanced gyrator with a relative timing error $|\Delta\tau|/T_m = 10\%$ and operational frequency $\omega = \omega_m$. The fundamental tone amplitude is $1 - 4|\Delta\tau|/T_m = 0.6$ and higher-order harmonics are enveloped by $4|\Delta\tau|/T_m \mathrm{sinc}(n\pi|\Delta\tau|/T_m)$. Expectedly, as the timing error $\Delta\tau$ approaches zero, residual even-order harmonics disappear, and the fundamental tone approaches full transmission. The fundamental-tone scattering parameters of the singly balanced gyrator can be found from the results in Appendix A as

$$S = \begin{bmatrix} 0 & \frac{2|\Delta\tau|}{T_m} e^{-j\omega\frac{T_m}{4}} + \left(1 - \frac{2|\Delta\tau|}{T_m}\right) e^{-j\omega\frac{3T_m}{4}} \\ \left(1 - \frac{2|\Delta\tau|}{T_m}\right) e^{-j\omega\frac{T_m}{4}} + \frac{2|\Delta\tau|}{T_m} e^{-j\omega\frac{3T_m}{4}} & 0 \end{bmatrix}. \tag{18}$$

From Eq. (18), we gather an important conclusion: impedance matching and nonreciprocal phase shift of a singly balanced gyrator at the fundamental frequency are immune to switch timing errors. On the other hand, the insertion loss, $1 - 4|\Delta\tau|/T_m$, increases linearly with the timing error. Figure 5 shows the scattering matrix as a function of input signal frequency and switch timing error. Furthermore, insertion loss increases as we depart from the frequency of optimal operation $(2k+1)\omega_m$, $k = 0, 1, 2, 3, \ldots$. In order to have an insertion loss of less than 3 dB, the resulting maximum timing error is 7.3%. In IC implementations, it is feasible to keep the timing errors well below these levels, as well as to include calibration circuitry that corrects such timing errors.

B. Differential gyrator

As shown in the previous subsection, a singly balanced gyrator exhibits full transmission over a bandwidth limited only by the dispersion of transmission lines in the absence of synchronization errors. However, the gyrator functionality, i.e., a nonreciprocal phase difference of π, is available only at discrete frequencies $\omega = (2k+1)\omega_m$, $k = 0, 1, 2, 3, \ldots$. This problem can be overcome

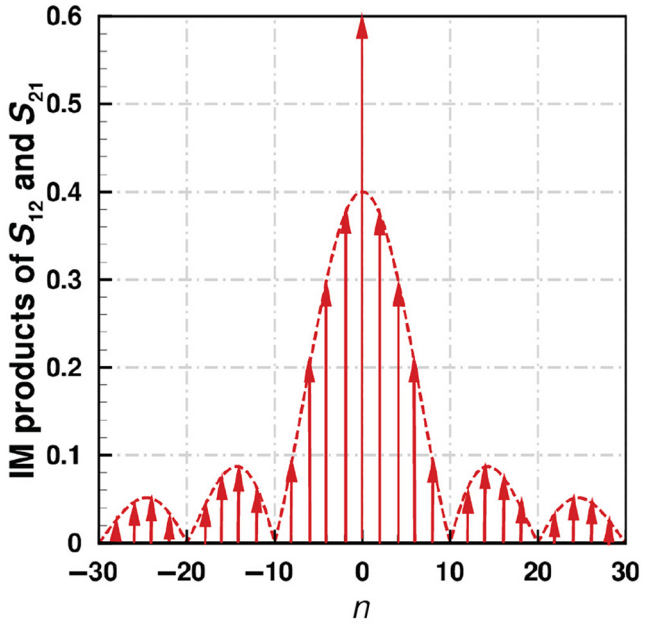

FIG. 4. Intermodulation (IM) products of a singly balanced gyrator with relative timing error $|\Delta\tau|/T_m = 0.1$. n stands for the order of harmonics and the y axis is the amplitude of each harmonics.

using a differential configuration, which exhibits a nonreciprocal π phase shift over an infinite bandwidth under ideal conditions (ideal switches, dispersion-free transmission lines, no timing errors). The circuit schematic is shown in Fig. 6. For excitation from port 1, the signal is fully transmitted through the network with a time delay $V_2^-(t) = V_1^+(t - T_m/4)$. For excitation from differential port 2, the signal is flipped due to the differential arrangement of the switches. Therefore, the transmitted signal is $V_1^-(t) = -V_2^+(t - T_m/4)$. The scattering parameters can be expressed as

$$S(\omega) = \begin{bmatrix} 0 & e^{-j\omega\frac{T_m}{4}+j\pi} \\ e^{-j\omega\frac{T_m}{4}} & 0 \end{bmatrix}. \tag{19}$$

The transmission is unitary, and the nonreciprocal phase difference is π at all frequencies, making it an ideal gyrator.

In the presence of switch desynchronization, the performance is deteriorated: for excitation from port 1, a major part of the signal overlapping with $\eta_1(t)$ in Fig. 3(c) passes through the network with time delay $T_m/4$, while a small desynchronized tail overlapping with $\eta_2(t)$ in Fig. 3(d) is transmitted through the gyrator with flipped polarity. For backward excitation from differential port 2, the large part of the signal overlapping with $\eta_1(t)$ in Fig. 3(c) is flipped, and a small tail overlapping with $\eta_2(t)$ in Fig. 3(d) propagates without flipping of the polarity. The above time-domain operation is described by the equations

$$V_2^-(t) = V_1^+\left(t - \frac{T_m}{4}\right)\eta_1(t) - V_1^+\left(t - \frac{T_m}{4}\right)\eta_2(t), \tag{20}$$

$$V_1^-(t) = 0, \tag{21}$$

$$V_1^-(t) = -V_2^+\left(t - \frac{T_m}{4}\right)\eta_1\left(t - \frac{T_m}{4}\right) + V_2^+\left(t - \frac{T_m}{4}\right)\eta_2\left(t - \frac{T_m}{4}\right), \tag{22}$$

$$V_2^-(t) = 0. \tag{23}$$

Again, here Eqs. (20)–(23) correspond to excitation from ports 1 and 2, respectively.

The corresponding scattering matrix for the fundamental tone, derived rigorously in Appendix A, reads

$$S = \begin{bmatrix} 0 & -\left(1 - \frac{4|\Delta\tau|}{T_m}\right)e^{-j\omega\frac{T_m}{4}} \\ \left(1 - \frac{4|\Delta\tau|}{T_m}\right)e^{-j\omega\frac{T_m}{4}} & 0 \end{bmatrix}. \tag{24}$$

Equation (24) indicates that the differential gyrator also maintains a zero return loss even in the presence of timing errors. In addition, the differential gyrator has the advantage of having a nonreciprocal phase response that is not affected by desynchronization, owing to the differentially arranged switches. Although the insertion loss is affected by the timing error, the impact is nondispersive, indicating that the bandwidth is not affected either.

III. ISOLATORS

In the previous section, we characterize singly balanced and differential gyrator designs by modulating the switch conductivity between zero and infinity. While this configuration can realize gyration and nonreciprocal phase shifts, nonreciprocal transmission magnitude cannot be realized with this strategy, because the circuit, in the absence of frequency conversion, is lossless, and it is impossible to realize isolation in lossless, linear devices. A two-port isolator design necessarily involves finite loss to absorb the energy in the direction of isolation [14]. In this section, we relax this assumption and discuss the design of singly balanced and ultrabroad-band doubly balanced isolators based on modulating the conductivity over a finite range, which allows the presence of absorption. We then investigate synchronization issues and remedy strategies are proposed to counterbalance these imperfections.

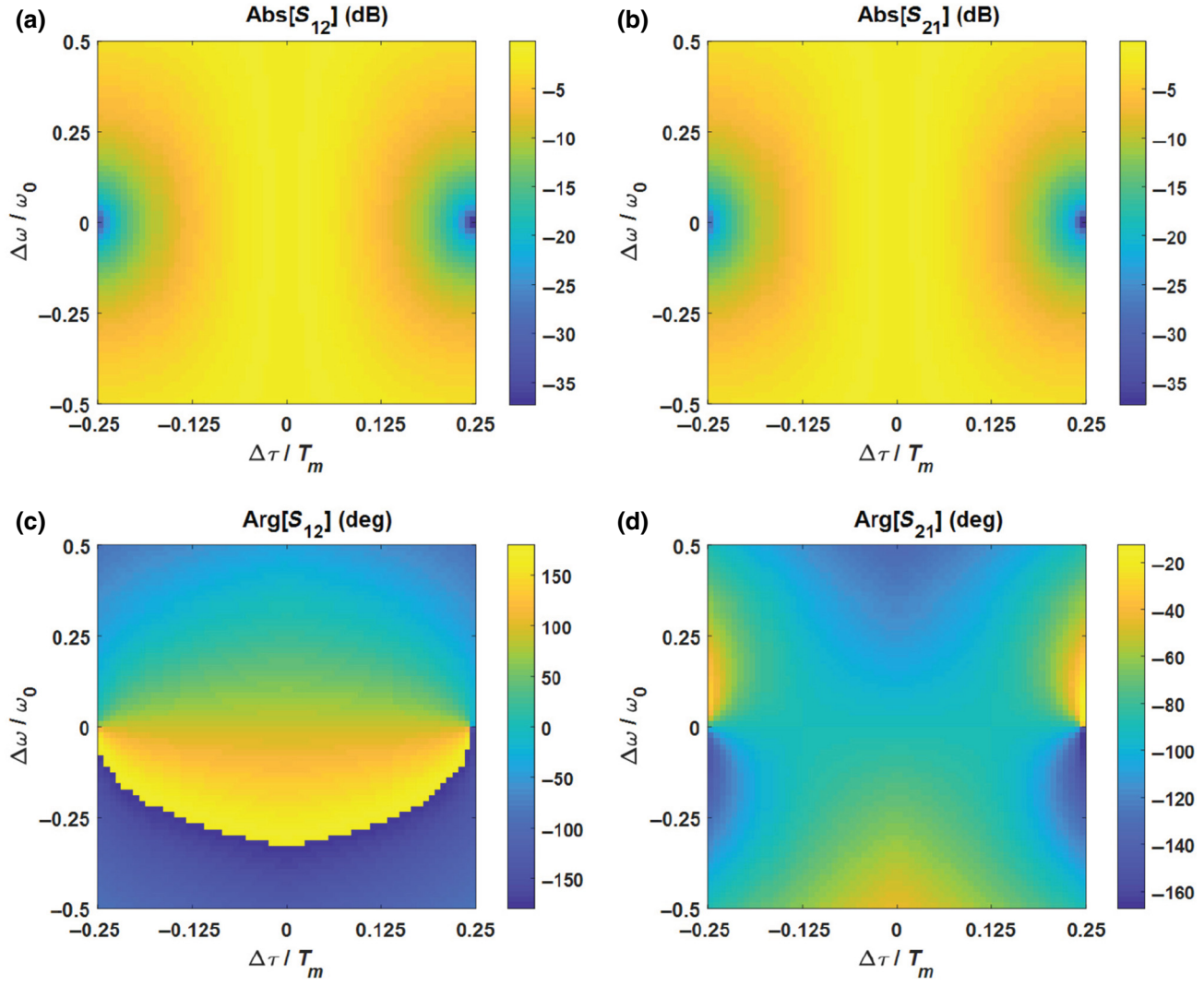

FIG. 5. Scattering properties of a singly balanced gyrator with timing error. (a) Magnitude of the backward transmission S_{12}; (b) magnitude of the forward transmission S_{21}; (c) phase of the backward transmission S_{12}; (d) phase of the forward transmission S_{21}. ω_0 is the operational frequency and $\Delta\omega$ is the input frequency shift.

A. Singly balanced isolator

Figure 7(a) shows an isolator design, based on a transmission line sandwiched between two modulated resistances, where the conductivity is modulated between infinity, i.e., perfect transmission, and a finite value R_m [20]. In time domain, the modulation follows the same pattern as in the case of the gyrator. By tracking the propagation of input signals through the system as in the gyrator case, the output signals can be expressed as

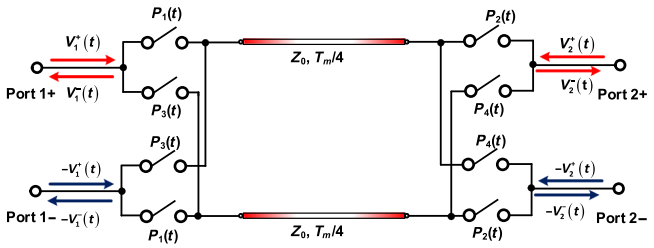

FIG. 6. Circuit schematic of the differential gyrator. Switching signals are the same as Fig. 1.

$$V_2^-(t) = V_1^+\left(t-\frac{T_m}{4}\right)P_1\left(t-\frac{T_m}{4}\right) + T^2V_1^+\left(t-\frac{T_m}{4}\right)\left[1-P_1\left(t-\frac{T_m}{4}\right)\right], \quad (25)$$

$$V_1^-(t) = \Gamma V_1^+(t)[1-P_1(t)] + \Gamma T V_1^+\left(t-\frac{T_m}{2}\right)\left[1-P_1\left(t-\frac{T_m}{2}\right)\right], \quad (26)$$

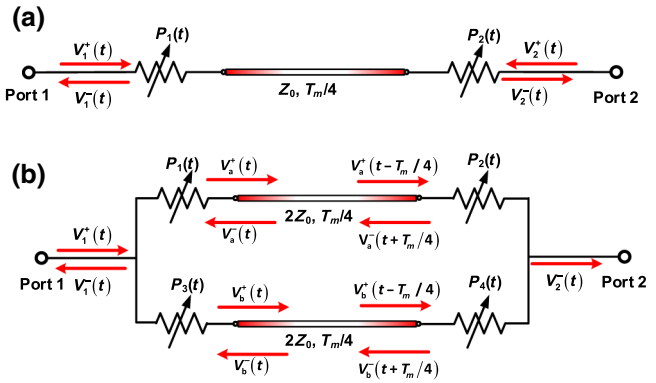

FIG. 7. Circuit schematic of the isolator. (a) Single-branch isolator, modulation signals P1 and P2 are the same as Fig. 1. (b) Singly balanced isolator, modulation signals P1, P2, P3, and P4 are the same as Fig. 1. The characteristic impedance of the transmission line is $2Z_0$.

$$V_1^-(t) = TV_2^+\left(t-\frac{T_m}{4}\right) + \Gamma^2 V_2^+\left(t-\frac{3T_m}{4}\right)P_2\left(t-\frac{3T_m}{4}\right), \tag{27}$$

$$V_2^-(t) = \Gamma V_2^+(t)[1-P_2(t)] + \Gamma T V_2^+\left(t-\frac{T_m}{2}\right)P_2\left(t-\frac{T_m}{2}\right), \tag{28}$$

where Eqs. (25) and (26) are the temporal responses for excitation at port 1, Eqs. (27) and (28) are the temporal responses for excitation at port 2, and $P_1(t)$ and $P_2(t)$ are the switching signals, provided in Fig. 1(c) (here, "0" stands for finite conductivity, namely resistance R_m, while "1" stands for infinite conductivity, i.e., perfect transmission). $\Gamma = R_m(R_m+2Z_0)^{-1}$ is the reflection coefficient when the resistance is R_m, and $T = 1-\Gamma$ is the corresponding transmission coefficient. Equations (25)–(28) simplify into Eqs. (1)–(4) if the resistance R_m approaches infinity ($\Gamma = 1$, $T = 0$), as expected. The scattering matrix for the fundamental tone is given by

$$S = \begin{bmatrix} \frac{\Gamma}{2}\left(1+Te^{-j\omega\frac{T_m}{2}}\right) & Te^{-j\omega\frac{T_m}{4}} + \frac{1}{2}\Gamma^2 e^{-j\omega\frac{3T_m}{4}} \\ \frac{1}{2}(1+T^2)e^{-j\omega\frac{T_m}{4}} & \frac{\Gamma}{2}\left(1+Te^{-j\omega\frac{T_m}{2}}\right) \end{bmatrix}. \tag{29}$$

The above result encompasses many interesting scenarios. When $\Gamma = 0$, it corresponds to the case in which the switch is always on, and hence we achieve a reciprocal response, $S_{12} = S_{21} = \exp(-j\omega T_m/4)$, and zero return loss, $S_{11} = S_{22} = 0$. When $\Gamma = 1$, the circuit is a single-branch gyrator, consistent with the previous section, with a return loss of 6 dB, $S_{11} = S_{22} = 1/2$, and nonreciprocal phase transmission [see Eq. (5)]. Interestingly, the same model can provide full isolation for appropriately selected values of Γ and T. In particular, if we require full isolation ($S_{12} = 0$), we find that it is obtained for $\omega = (2k+1)\omega_m$, $k = 0, 1, 2, 3, \ldots$, and $R_m = R_{\rm iso} = 2(1+\sqrt{3})Z_0$. Isolation in this case is the result of destructive interference at port 1 of the signals that reach this port after 1 and 3 paths through the transmission line, as evidenced by the phase of the two terms in the expression of S_{12}. Under these circumstances, we find that return and insertion loss are given by $|S_{11}| = |S_{22}| = 2-\sqrt{3}$ and $|S_{21}| = 2(2-\sqrt{3})$, respectively.

It is interesting to note that these quantities do not depend on the parameters of the system (T_m and Z_0), but instead are inherent properties of the considered circuit topology. Figures 8(a) and 8(b) plot amplitude and phase of the scattering parameters for this isolator design. At $\omega = \omega_m$ and $\omega = 3\omega_m$, full isolation is achieved, whereas at $\omega = 2\omega_m$ we find reciprocal transmission $S_{21} = S_{12} = -2(2-\sqrt{3})$. It is interesting that the transmission amplitude in the forward direction is the same for all frequencies, which can also be seen from Eq. (29). The forward-propagating signal always experiences a finite reflection Γ, due to the finite resistance value R_m. In order to eliminate this return loss, we consider a differential topology [Fig. 7(b)], in which the characteristic impedance of the two parallel transmission lines is tuned to $2Z_0$ to match the port impedance. The reflection coefficient for each individual signal pass in this case is frequency dependent, and a rigorous temporal analysis is presented in Appendix B. The S parameters at $\omega = (2k+1)\omega_m$ become

$$S|_{\omega=(2k+1)\omega_m} = \begin{bmatrix} 0 & j(-1)^{k+1}(\mathscr{T}^2-\mathscr{R}^2) \\ j(-1)^{k+1} & 0 \end{bmatrix}, \tag{30}$$

where $\mathscr{T} = 8Z_0(R_m+8Z_0)^{-1}$ and $\mathscr{R} = R_m(R_m+8Z_0)^{-1}$ are the transmission and reflection coefficients experienced by the signal during each pass. Interestingly, the above equation indicates that impedance is automatically matched at operation frequencies. The condition for complete backward isolation is $\mathscr{R} = \mathscr{T}$, thereby leading to an isolation resistance $R_m = R_{\rm iso} = 8Z_0$ for full isolation. $R_{\rm iso}$ marks the boundary of the nonreciprocal phase difference for transmission, where $R_m < R_{\rm iso}$ indicates zero phase difference between S_{21} and S_{12}, and $R_m > R_{\rm iso}$ provides π phase difference. In the extreme case $R_m \to 0$, the design recedes to a transmission line with characteristic impedance Z_0. In the extreme scenario $R_m \to \infty$, the circuit becomes the differential gyrator we discussed in the previous section.

To further validate our temporal analysis across the full spectrum band, we use the composite FSM method, as

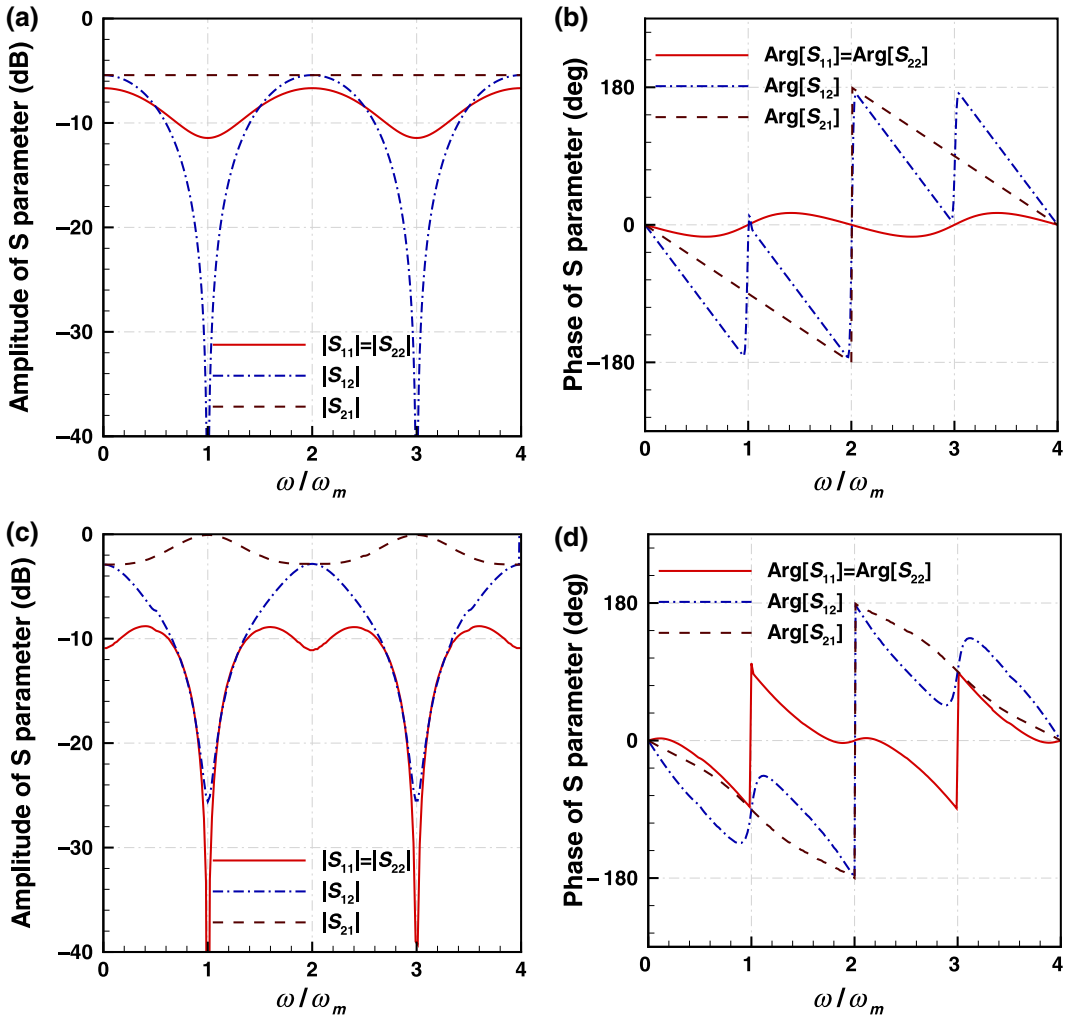

FIG. 8. *S* parameter of the isolator. (a) Magnitude of the *S* parameter of a single-branch isolator. (b) Phase of the *S* parameter of a single-branch isolator. (c) Magnitude of the *S* parameter of a singly balanced branch isolator. (d) Phase of the *S* parameter of a singly balanced isolator.

described in Ref. [37], to compute the scattering parameters [Figs. 8(c) and 8(d)] for isolation resistance $R_{\rm iso} = 8Z_0$. Our numerical results from composite FSM method are in excellent agreement with the analytical results and also with numerical simulations using Keysight ADS, which are not shown here for space limitations.

Now, we consider a single-branch isolator with a small timing error, where $P_2(t) = P_1(t - T_m/4 - \Delta\tau)$ and $|\Delta\tau| < T_m/4$. A rigorous temporal and frequency analysis, similar to the one presented for the gyrators in the previous section, is performed in Appendix B. We obtain the *S* parameters

$$S = \begin{bmatrix} \frac{\Gamma}{2}\left(1 + Te^{-j\omega\frac{T_m}{2}}\right) & \left(T + \frac{\Gamma^2|\Delta\tau|}{T_m}\right)e^{-j\omega\frac{T_m}{4}} + \left(\frac{1}{2}\Gamma^2 - \frac{\Gamma^2|\Delta\tau|}{T_m}\right)e^{-j\omega\frac{3T_m}{4}} \\ \left(\frac{1+T^2}{2} - \frac{\Gamma^2|\Delta\tau|}{T_m}\right)e^{-j\omega\frac{T_m}{4}} + \frac{\Gamma^2|\Delta\tau|}{T_m}e^{-j\omega\frac{3T_m}{4}} & \frac{\Gamma}{2}\left(1 + Te^{-j\omega\frac{T_m}{2}}\right) \end{bmatrix}. \tag{31}$$

Interestingly, the timing error of the second switch has no influence on the return loss at either port. This is a major advantage of the synchronized loss modulation design. Assuming no timing error, when port 1 is excited by an input signal $\exp(j\omega t)$, it passes through the transmission line and the second switch consecutively during the first half of the modulation period. The signal in the second half of the modulation period is partially reflected at port 1, transported through the delay line, reflected at port 2, and, finally, partially transmits through the first switch. The return signal is essentially a superposition of the first-time reflection and another second-time reflection with a delay $T_m/4$, leading to a phase delay $\exp(-j\omega T_m/2)$ in the second term of S_{11} and S_{22}. In the presence of a timing error, the second reflection (the one happening when switch 1 is open) occurs over the time $T_m/2 - \Delta\tau$, instead of $T_m/2$. However, there is an extra reflection with the same scaling factor ΓT and time delay $T_m/2$, occurring over an additional time $\Delta\tau$ right after switch 1 is closed, during which the signal finds switch 2 in the open state. This additional reflection compensates for the reduced duration of the main reflection at the fundamental tone, leading to the same reflection coefficient as when there is no timing error, although it affects the intermodulation products. In other words, the sole effect of the timing error is redistribution of power among the intermodulation harmonics, which would otherwise be ideal [39]. For the transmitted signals, the timing error results in a signal tail bouncing back and forth inside the delay line before finding its way out, leading to an extra average insertion loss $\Gamma^2|\Delta\tau|/T_m$ over the modulation period, as shown in S_{12} and S_{21} in Eq. (31). In Fig. 9, we plot scattering parameters computed using the composite FSM method, which show good agreement with analytical results from Eq. (31) and our theoretical analysis in the previous paragraph. To maintain −20-dB isolation, the relative timing error should be less than 10.9%. The corresponding fractional bandwidth is 12.5%.

Another degree of freedom in the isolator design is the resistor value, which we can tune to optimize the isolation in the presence of timing error. Figure 10 shows the modification of the scattering parameters as we vary $\Delta\tau$ and R_m, as from Eq. (31). As seen in Fig. 10(b), the isolation map shows a dip for certain combinations of $\Delta\tau$ and R_m. An abrupt phase jump in S_{12} shown in Fig. 10(e) indicates that ideal isolation is indeed possible. We closely study the backward propagation coefficient in Eq. (31), and derive an analytical expression for optimal resistance as a function of $\Delta\tau$ and R_m:

$$R_{\text{optimal}} = 2Z_0\left[1+\sqrt{3-\frac{8|\Delta\tau|}{T_m}}\right]\left(1-\frac{4|\Delta\tau|}{T_m}\right)^{-1}, \tag{32}$$

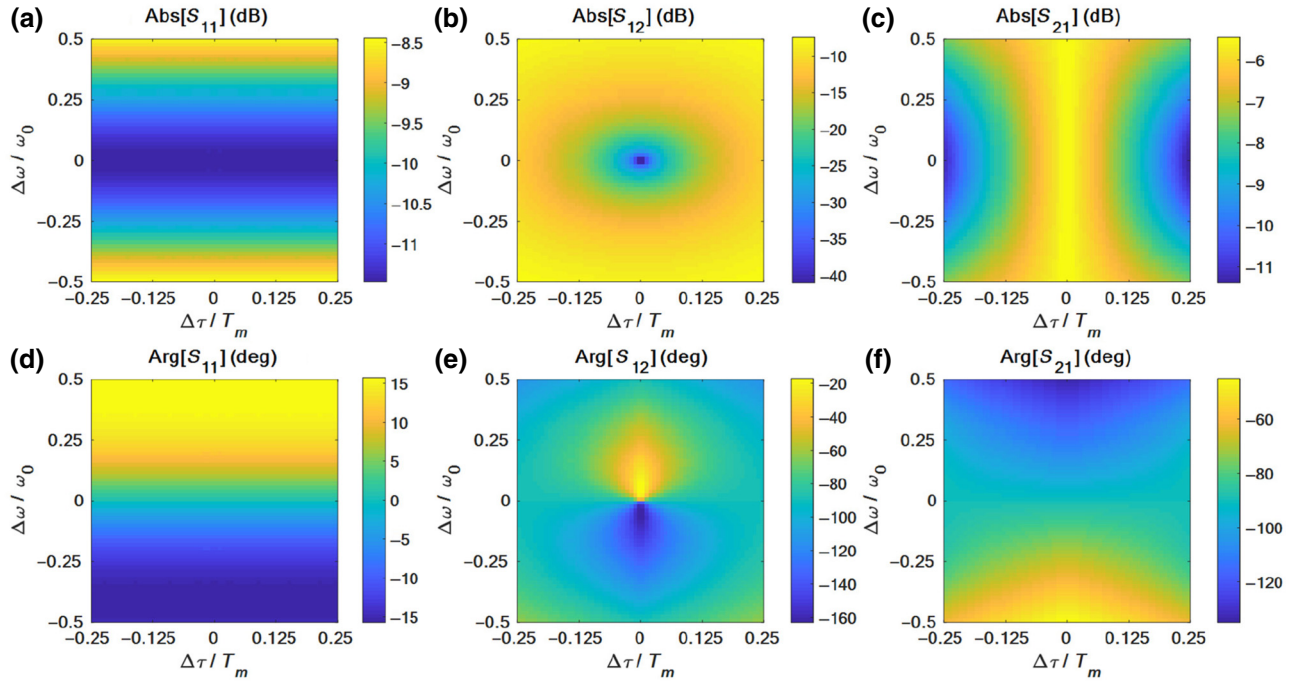

FIG. 9. S parameter of a single-branch isolator with timing error. (a) Magnitude of the return loss S_{11} of a single-branch isolator. (a) Magnitude of the isolation S_{12} of a single-branch isolator. (c) Magnitude of the transmission S_{21} of a single branch isolator. (d) Phase of the isolation S_{11} of a single-branch isolator. (e) Phase of the isolation S_{12} of a single-branch isolator. (f) Phase of the transmission S_{21} of a single-branch isolator.

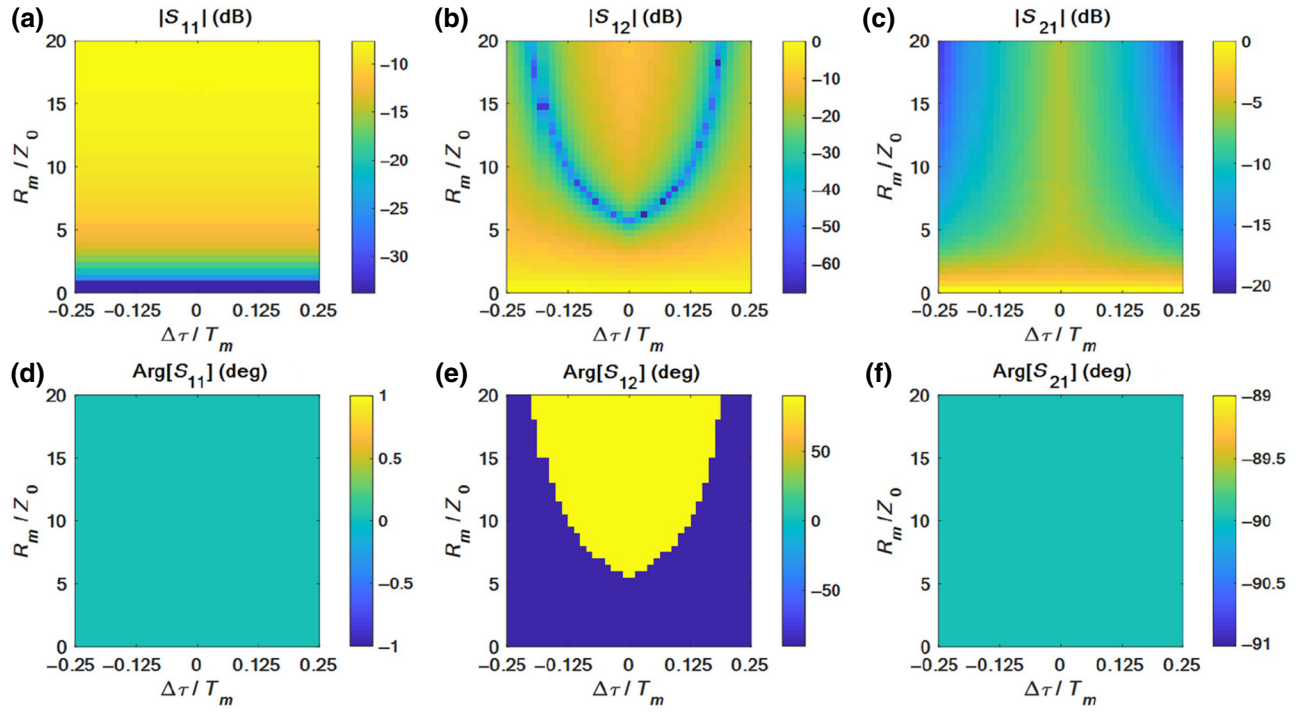

FIG. 10. Variation of S parameters of the single-branch isolator in the presence of timing error, as a function of the switch resistance. (a) Magnitude of the return loss $S_{11} = S_{22}$ of a single-branch isolator. (a) Magnitude of the isolation S_{12} of a single-branch isolator. (c) Magnitude of the transmission S_{21} of a single-branch isolator. (d) Phase of the return loss $S_{11} = S_{22}$ of a single-branch isolator. (e) Phase of the isolation S_{12} of a single-branch isolator. (f) Phase of the transmission S_{21} of a single-branch isolator.

which perfectly matches our numerical simulation and ensures ideal isolation. The insertion loss grows as we tune the resistor to improve isolation upon a given timing error, as shown in Fig. 10(c), implying a trade-off between isolation and insertion loss as the timing error grows.

The singly balanced isolator simultaneously enables perfect impedance matching, full transmission, and full isolation at its operation frequencies. Figure 11 shows the scattering parameters plotted versus timing error in the proximity of the operation frequency. As we see in Fig. 11(a), the return loss is immune to synchronization issues and it remains as low as 40 dB when relative timing error varies from -0.25 to 0.25. The sharp phase transition from $-90°$ to $90°$ along $\Delta\omega = 0$ in Fig. 11(d) is consistent with the region with zero return loss. At the operational frequency, the scattering matrix can be written as

$$S|_{\omega=(2k+1)\omega_m} = \begin{bmatrix} 0 & j(-1)^{k+1}\left[-\mathscr{R}^2 + \mathscr{T}^2 + \dfrac{2|\Delta\tau|(1+\mathscr{R}^2-\mathscr{T}^2)}{T_m}\right] \\ j(-1)^{k+1}\left[1 - \dfrac{2|\Delta\tau|(1+\mathscr{R}^2-\mathscr{T}^2)}{T_m}\right] & 0 \end{bmatrix}. \quad (33)$$

This equation describes many interesting scenarios. For instance, $\mathscr{R} = 1$ corresponds to a desynchronized gyrator [Eq. (18)], $|\Delta\tau| = 0$ represents an ideally synchronized isolator [Eq. (30)], $|\Delta\tau| = 0$ and $\mathscr{R} = 1$ denote a perfect gyrator [Eq. (8)] and $\mathscr{R} = 0$ implies a reciprocal transmission line. The insertion loss exhibits a linear decay $1 - 2|\Delta\tau|/T_m$ with synchronization issues, and the isolation increases linearly with the relative delay $2|\Delta\tau|/T_m$

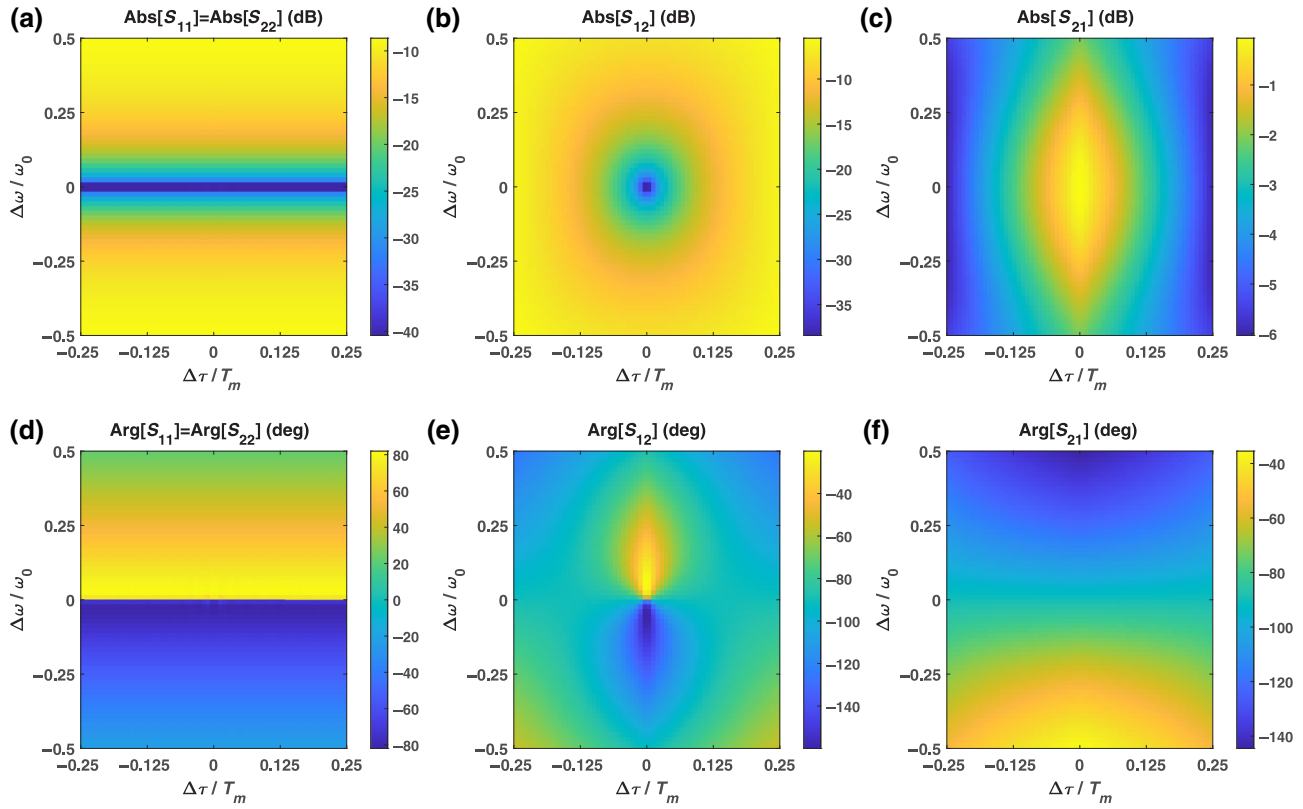

FIG. 11. S parameter of the singly balanced isolator with timing error. (a) Magnitude of the return loss S_{11} of a singly balanced branch isolator. (b) Magnitude of the isolation S_{12} of a singly -balanced branch isolator. (c) Magnitude of the transmission S_{21} of a singly balanced branch isolator. (d) Phase of the return loss S_{11} of a singly balanced branch isolator. (d) Phase of the isolation S_{12} of a balanced singly branch isolator. (c) Phase of the transmission S_{21} of a singly balanced branch isolator.

when $\mathscr{R} = \mathscr{T}$. To maintain a 3-dB insertion loss and 20-dB isolation, the relative timing error should stay within 5%. Backward transmission can be made identically zero (i.e., infinite isolation), when the open switch resistance is tuned to the optimal value

$$R_{\text{optimal}} = 8Z_0\left(1 - 4\left|\frac{\Delta\tau}{T_m}\right|\right)^{-1}. \tag{34}$$

By tuning the resistor to this value, the system ensures ideally infinitely isolation and transmission loss below 3 dB, even with 11% relative timing error, readily achievable in IC implementations. Figure 12 shows this trade-off in the case of the double branch isolator in the presence of timing errors.

B. Ultrabroad-band isolator

Another way to obtain an isolator is to add a differential dissipative port in parallel to port 1 in a singly balanced gyrator, which can absorb the energy for backward excitation from port 2 (see Fig. 13). For excitation from port 1, the circuit behaves like a quarter-wavelength transmission line: $V_2^-(t) = V_1^+(t - T_m/4)$. For excitation from port 2, during the first half of the modulation period, the signal passes through switch P_2 and meets an open circuit at port 1. However, switch P_3 is on and port 3 is loaded with a characteristic impedance Z_0. Therefore, the signal is fully absorbed at port 3. For the second half of the modulation period, the signal is transmitted through switches P_4 and P_1, when excited from port 1, and is again fully dissipated at port 3, when excited from port 2. The scattering parameters of this isolator are

$$S(\omega) = \begin{bmatrix} 0 & 0 \\ e^{-j\omega\frac{T_m}{4}} & 0 \end{bmatrix}. \tag{35}$$

The operational bandwidth of this isolator is ideally infinite compared with the singly balanced isolator, which operates at a discrete set of frequencies.

Consider now synchronization issues in this isolator. When port 1 is excited by a monochromatic signal $e^{j\omega t}$, most of the signal overlapping with $\eta_1(t)$ in Fig. 3(c) passes through the transmission line and reaches port 2.

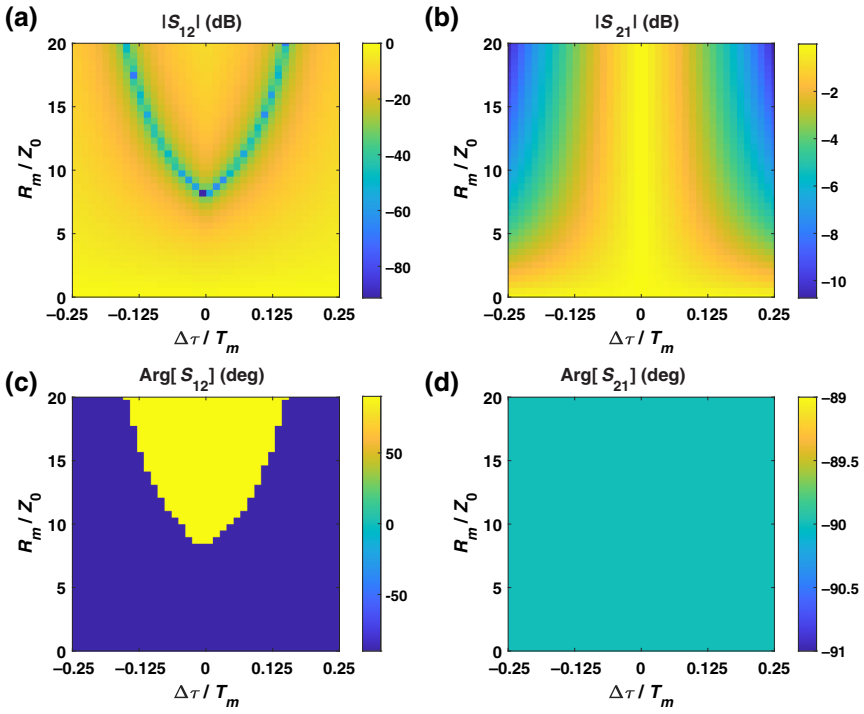

FIG. 12. Variation of the singly balanced isolator in the presence of timing error, as a function of the switch resistance. (a) Magnitude of the isolation S_{12} of a singly balanced branch isolator. (c) Magnitude of the transmission S_{21} of a singly balanced branch isolator. (d) Phase of the isolation S_{12} of a singly balanced branch isolator. (c) Phase of the transmission S_{21} of a singly balanced branch isolator.

A small tail of the signal, with duration $\Delta\tau$, overlaps with $\eta_2(t)$ in Fig. 3(d) and is reflected to port 3, where it is absorbed. Hence, the transmitted signal is $V_2^-(t) = V_1^+(t - T_m/4)\eta_1(t)$. Since no signal is reflected to the input port, return loss is zero. For excitation from port 2, most of the signal overlaps with $\eta_1(t)$ in Fig. 3(c) and is absorbed at port 3, apart from a small tail overlapping with $\eta_2(t)$ in Fig. 3(d), which passes through port 1, leading to a transmitted signal $V_1^-(t) = V_2^+(t - T_m/4)\eta_2(t - T_m/4)$. The scattering matrix of the fundamental tone is extracted from Eq. (B20)–(B23) in Appendix B:

$$S(\omega) = \begin{bmatrix} 0 & \frac{2|\Delta\tau|}{T_m} e^{-j\omega\frac{T_m}{4}} \\ \left(1 - \frac{2|\Delta\tau|}{T_m}\right) e^{-j\omega\frac{T_m}{4}} & 0 \end{bmatrix}. \quad (36)$$

The timing error affects only isolation and insertion loss through the term $2|\Delta\tau|/T_m$. Intermodulation products of this isolator with timing error are plot in Fig. 14, showing

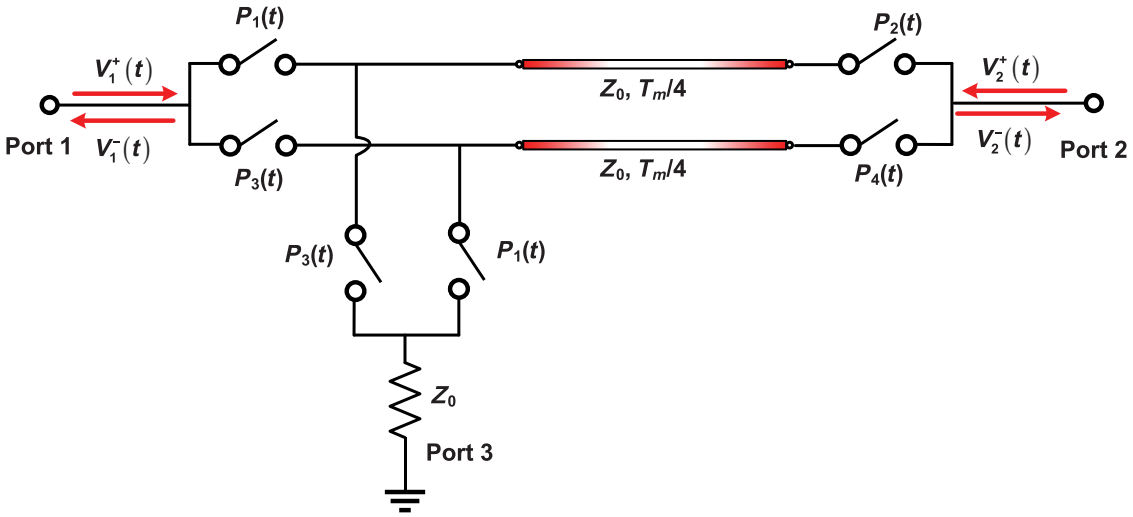

FIG. 13. Circuit schematic of the ultrabroad-band isolator. Modulation signals P1, P2, P3, and P4 are the same as Fig. 1.

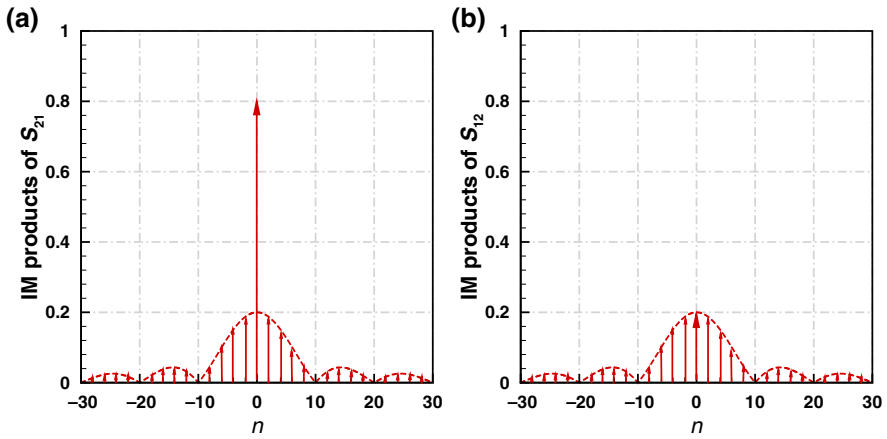

FIG. 14. IM products of an ultrabroadband isolator with relative timing error $|\Delta\tau|/T_m = 0.1$. n stands for the order of harmonics and y axis is the amplitude of each harmonics.

little influence on the overall spectrum of the transmitted signal for moderate delays.

IV. CIRCULATORS

In this section, we present three circulator designs and investigate their performance in the presence of synchronization issues. The first design is a singly balanced circulator, which is based on an extension of the singly balanced gyrator described in Sec. II. The second circulator is a doubly balanced circulator based on a differential gyrator. The third circulator is based on the ultrabroad-band isolator design discussed in the previous section, where we remove the load Z_0 and add port 3 in its replacement.

A. Singly balanced circulator

A circulator is a multiport device that routes the signal with a given handedness from port to port. One approach to obtain a circulator is to embed a gyrator in a transmission-line ring, as in Fig. 15, where we use the balanced gyrator from Sec. II as the basic element to yield nonreciprocity. Isolation at the various ports arises due to destructive interference from the reciprocal and nonreciprocal paths in the loop. At frequency $\omega = (2k+1)\omega_m$, $k = 0,\ 1,\ 2,\ 3\ldots$, the gyrator provides $(2k+1)3\pi/2$ and $(2k+1)\pi/2$ phases in the two opposite directions. If a monochromatic signal $e^{j\omega t}$ enters from port 1, it is split into two signals with identical amplitudes. One takes the path via port 3, and the other goes directly from port 1 to port 2. These signals experience a relative π phase shift and interfere destructively at port 2, leading to full isolation, $S_{21} = 0$. On the other hand, at port 3 these signals interfere constructively, leading to a unitary transmission, $S_{31} = -j$. We can analyze the responses of excitation at port 2 and port 3 in a similar way and obtain

$$S|_{\omega=(2k+1)\omega_m} = \begin{bmatrix} 0 & -1 & 0 \\ 0 & 0 & j(-1)^{k+1} \\ j(-1)^{k+1} & 0 & 0 \end{bmatrix}. \quad (37)$$

A more thorough theoretical analysis is presented in Appendix C, where the responses at all frequencies are derived. This circulator is essentially asymmetric, since the transmission coefficients are not identical: $S_{31} = S_{23} \neq S_{12}$. The directionality of the circulator can be reversed by reversing the nonreciprocal phase response of the gyrator.

In order to validate our analysis, we numerically evaluate the scattering parameters using the composite FSM method. Figures 16(a) and 16(b) demonstrate amplitudes and phases of scattering parameters at port 1. As we see, the circulator exhibits isolation in S_{21} larger than 40 dB

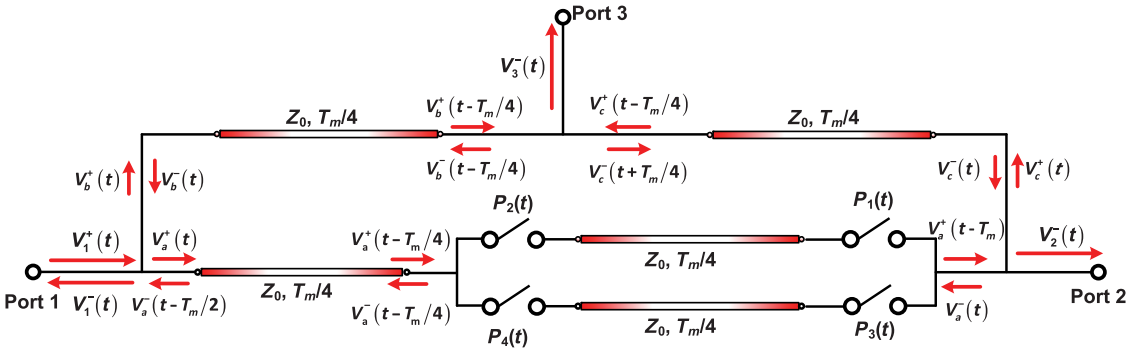

FIG. 15. Singly balanced circulator. Modulation signals P1, P2, P3, and P4 are the same as Fig. 1.

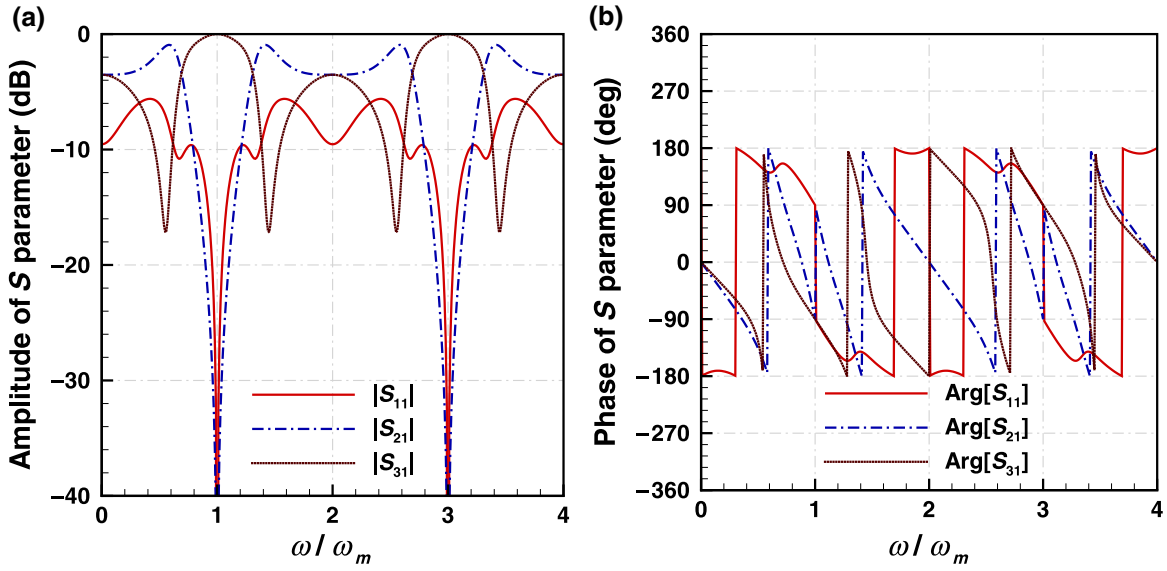

FIG. 16. S parameter of the singly balanced circulator. (a) Magnitude of the S parameter at port 1 of a singly balanced circulator. (b) Phase of the S parameter at port 1 of a singly balanced circulator.

and full transmission at frequency $\omega = \omega_m$ and $\omega = 3\omega_m$. The phase discontinuity of S_{21} and the $-\pi/2$ phase shift of S_{31} at $\omega = \omega_m$ and $\omega = 3\omega_m$ are consistent with theoretical predictions in Eq. (37). The scattering matrix accounting for timing errors is

$$S|_{\omega=(2k+1)\omega_m} = \begin{bmatrix} 0 & -\left(1-2\frac{|\Delta\tau|}{T_m}\right) & j(-1)^{k+1}\frac{2|\Delta\tau|}{T_m} \\ -\frac{2|\Delta\tau|}{T_m} & 0 & j(-1)^{k+1}\left(1-\frac{2|\Delta\tau|}{T_m}\right) \\ j(-1)^{k+1}\left(1-\frac{2|\Delta\tau|}{T_m}\right) & j(-1)^{k+1}\frac{2|\Delta\tau|}{T_m} & 0 \end{bmatrix}. \tag{38}$$

From Eq. (38), we see that the insertion loss and isolation deteriorate as the timing error increases. The return loss remains identically zero, unaffected by the presence of synchronization issues. For the insertion loss to be smaller than 3 dB and the isolation larger than 20 dB, the timing error needs to be smaller than 5%. A full picture of the S parameters for excitation from port 1 versus the timing error and input frequency is provided in Fig. 17 by using FSM numerical simulations.

B. Doubly balanced circulator

A circulator can also be designed leveraging the differential gyrator where the nonreciprocal phase response has an ideally infinite bandwidth. Figure 18 demonstrates such a design. Due to the similarity between doubly and singly balanced circulator design, the scattering parameters at frequencies $\omega = (2k+1)\omega_m$, $k = 0,\ 1,\ 2,\ 3\ldots$ are identical to Eq. (37). However, the responses at other frequencies are slightly different due to the different phase response in the gyrator. A detailed and rigorous theoretical analysis is presented in Appendix C. Our results indicate that doubly balanced circulator offers a larger bandwidth compared with the singly balanced circulator. We also confirm our theoretical results using FSM numerical methods and plot the amplitude and phase of scattering parameters in Fig. 19 for the case when port 1 is excited.

As timing error exists in the device, the scattering parameters at the operational frequencies are

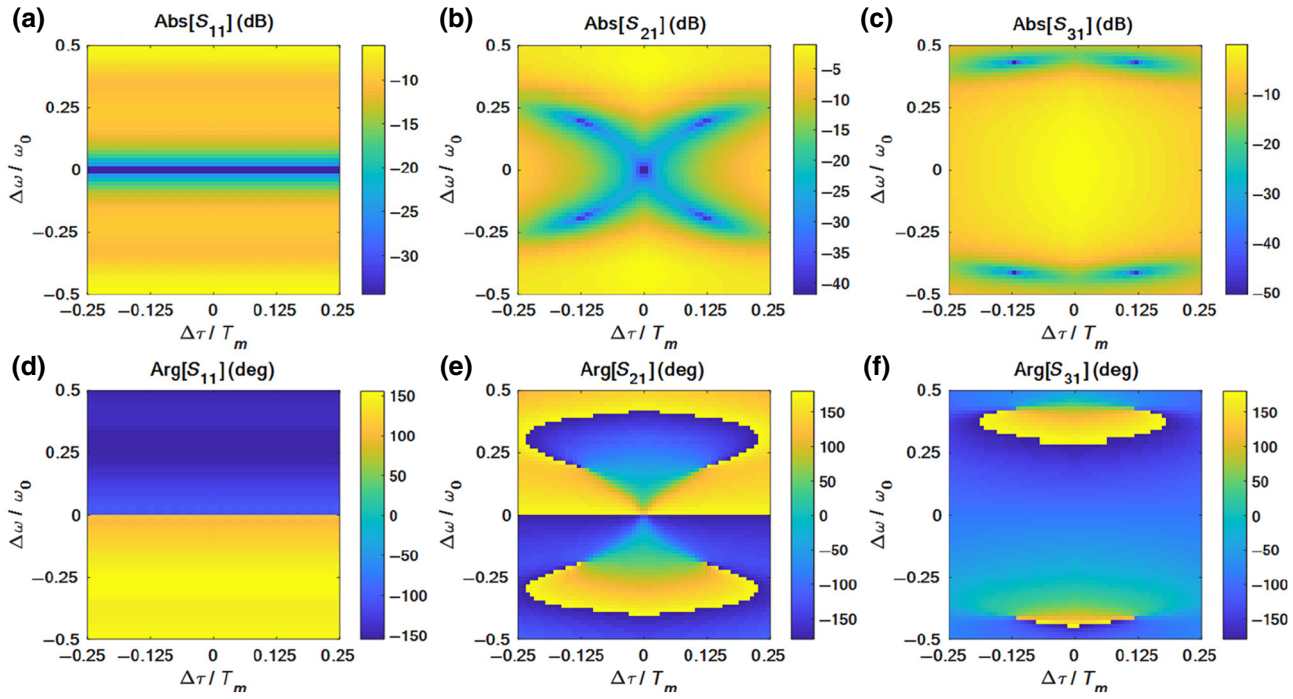

FIG. 17. S parameter of a singly balanced circulator with timing error. (a) Magnitude of the return loss S_{11} of a singly balanced circulator. (b) Magnitude of the isolation S_{21} of a singly balanced circulator. (c) Magnitude of the transmission S_{31} of a singly balanced circulator. (d) Phase of the return loss S_{11} of a singly balanced circulator. (e) Phase of the isolation S_{21} of a singly balanced circulator. (f) Phase of the transmission S_{31} of a singly balanced circulator.

$$S|_{\omega=(2k+1)\omega_m} = \begin{bmatrix} 0 & -\left(1-2\frac{|\Delta\tau|}{T_m}\right) & j(-1)^{k+1}\frac{2|\Delta\tau|}{T_m} \\ -\frac{2|\Delta\tau|}{T_m} & 0 & j(-1)^{k+1}\left(1-\frac{2|\Delta\tau|}{T_m}\right) \\ j(-1)^{k+1}\left(1-\frac{2|\Delta\tau|}{T_m}\right) & j(-1)^{k+1}\frac{2|\Delta\tau|}{T_m} & 0 \end{bmatrix}, \tag{39}$$

which are identical to the circulator based on the singly balanced gyrator in Eq. (38).

C. Ultrabroad-band circulator

A circulator can also be obtained by adding a differential port 3 in parallel with port 1 in the ultrabroad-band isolator design, as sketched in Fig. 20. The time-domain analysis here is quite straightforward. For excitation from port 1, the signal passes through the transmission line with time delay $T_m/4$ and arrives at port 2: $V_2^-(t) = V_1^+(t - T_m/4)$. For excitation from port 2, the signal reaches port 3 with a quarter-period delay: $V_3^-(t) = V_2^+(t - T_m/4)$. For excitation from port 3, the signal passes through the transmission line, reflects at port 2 and arrives at port 1 with a delay $T_m/2$: $V_1^-(t) = V_3^+(t - T_m/2)$. The scattering parameters of this ultrabroad-band circulator are

$$S(\omega) = \begin{bmatrix} 0 & 0 & e^{-j\omega\frac{T_m}{2}} \\ e^{-j\omega\frac{T_m}{4}} & 0 & 0 \\ 0 & e^{-j\omega\frac{T_m}{4}} & 0 \end{bmatrix}. \tag{40}$$

Consider now the case of synchronization delays: when excitation is applied to port 1, most of the signal passes through the transmission line and reaches port 2, apart from a small tail that is reflected to port 3 with a delay $T_m/2$. The output signals at ports 2 and 3 are $V_2^-(t) = V_1^+(t - T_m/4)\eta_1(t)$ and $V_3^-(t) = V_1^+(t - T_m/2)\eta_2(t - T_m/4)$, respectively, where $\eta_1(t)$ and $\eta_2(t)$ are the pulse sequences in Figs. 3(c) and 3(d). We perform similar analyses on ports 2 and 3 and obtain the following scattering matrix in the presence of a timing error:

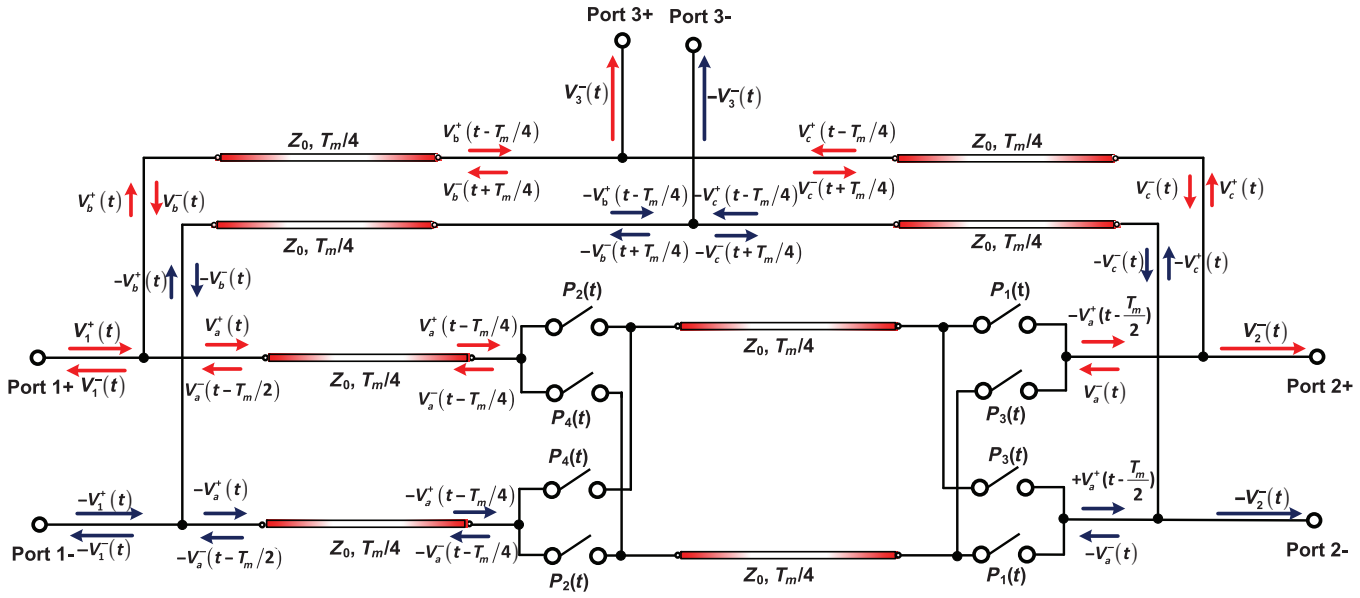

FIG. 18. Doubly balanced circulator. Modulation signals P1, P2, P3, and P4 are the same as Fig. 1.

$$S(\omega) = \begin{bmatrix} 0 & \frac{2|\Delta\tau|}{T_m} e^{-j\omega\frac{T_m}{4}} & \left(1 - \frac{2|\Delta\tau|}{T_m}\right) e^{-j\omega\frac{T_m}{2}} \\ \left(1 - \frac{2|\Delta\tau|}{T_m}\right) e^{-j\omega\frac{T_m}{4}} & 0 & \frac{2|\Delta\tau|}{T_m} e^{-j\omega\frac{T_m}{4}} \\ \frac{2|\Delta\tau|}{T_m} e^{-j\omega\frac{T_m}{2}} & \left(1 - \frac{2|\Delta\tau|}{T_m}\right) e^{-j\omega\frac{T_m}{4}} & 0 \end{bmatrix}. \tag{41}$$

It is seen that the timing error has no effect on the return loss also in this case, while it increases the insertion loss and reduces isolation by a factor of $2|\Delta\tau|/T_m$. Equation (41) holds for any frequency, in contrast to Eq. (38), which holds only at frequencies $\omega = (2k+1)\omega_m$, consistent with the fact that the singly balanced circulator has a limited bandwidth, whereas this design offers, in principle infinite bandwidth, only limited by the dispersion of the transmission lines and finite fall and rise times of the switches.

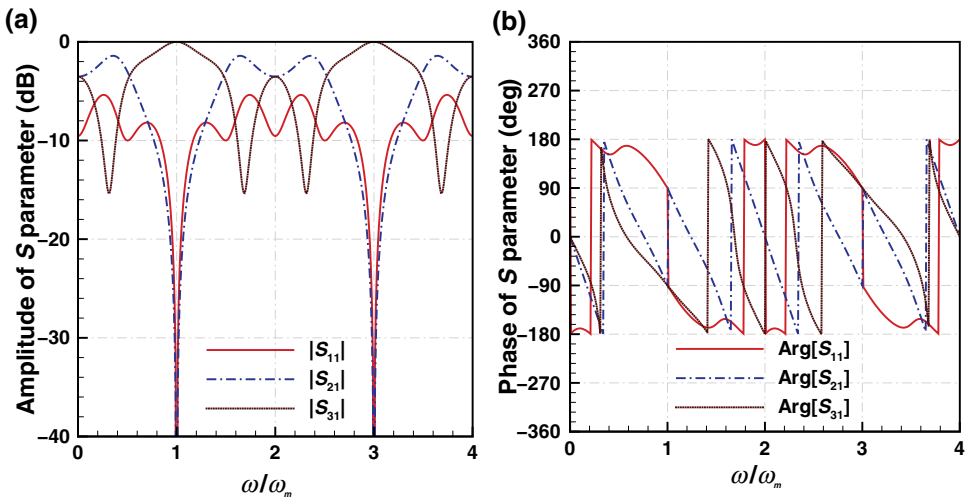

FIG. 19. S parameter of the doubly balanced circulator. (a) Magnitude of the S parameter at port 1 of a singly balanced circulator. (b) Phase of the S parameter at port 1 of a singly balanced circulator.

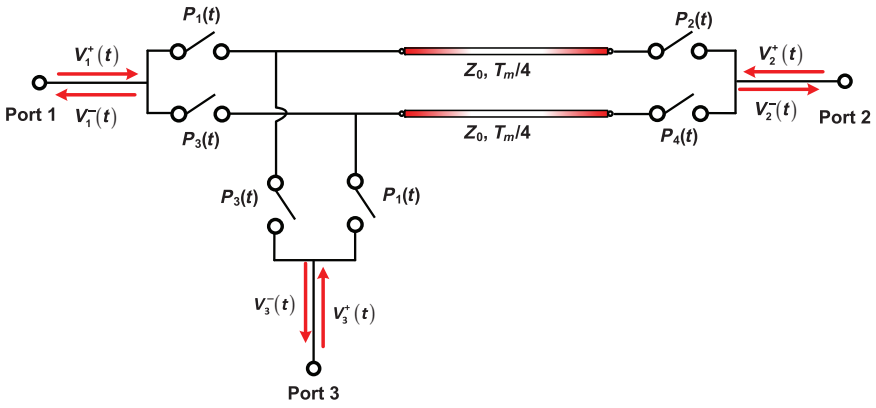

FIG. 20. Circuit schematic of the ultra-broad-band circulator. Modulation signals P1, P2, P3, and P4 are the same as Fig. 1.

V. CASE STUDIES ON REALISTIC IMPLEMENTATIONS

In this section, we provide a case study of the differential circulator implementation to validate our analysis. Monte Carlo simulations of the clock is performed and compared with our theoretical derivations in previous sections.

A. 60 GHz doubly balanced circulator

A 60-GHz CMOS circulator is implemented in a 45-nm SOI CMOS process using the doubly balanced switched-bandpass filter configuration. Theoretically, the switched-transmission-line structure has no loss and infinite bandwidth. In practice, however, losses are limited by the switch ON resistance R_{on} and its OFF parasitic capacitance C_{off}, and the dispersion in the transmission line. In Ref. [33], we recognized that for large f_{in}/f_m ratios, where f_{in} is the input rf signal frequency and f_m is the modulation signal frequency, the significant mixing products are centered around the input frequency f_{in}. Therefore, a bandpass filter (BPF) with quarter-wave group delay is enough to preserve them. The BPF is designed to absorb larger parasitic capacitances, allowing for a lower R_{on}, while still allowing enough bandwidth in the BPF to sustain the dominant mixing products, thus allowing low R_{on} loss as well as low Bragg loss. It is shown that at 60 GHz, the loss and power handling of the circulator can be improved by 1.3 and 9 dB, respectively, by using the switched-bandpass-filter approach. For 60-GHz operation, the switches are modulated at 8.6 GHz ($f_{in}/f_m = 7$). Figure 22(a) shows the 60-GHz circulator implemented in 45-nm SOI CMOS. Measured insertion losses are 3.6 dB and 3.1 dB insertion loss for TX-to-ANT and ANT-to-RX paths, respectively. Their sum degrades by 2 dB over a bandwidth of 6.8 GHz, and TX-to-RX isolation is >20 dB for this entire frequency range. Near the center frequency, the isolation is >40 dB over a bandwidth of 1.3 GHz. The clocking circuitry of the circulator consists of fine-phase-tuning varactors, a two-stage polyphase filter generating the differential I/Q signals, and self-biased pseudo-differential inverter chains. The gain of the final buffer is boosted using inductive peaking to generate the square clocks.

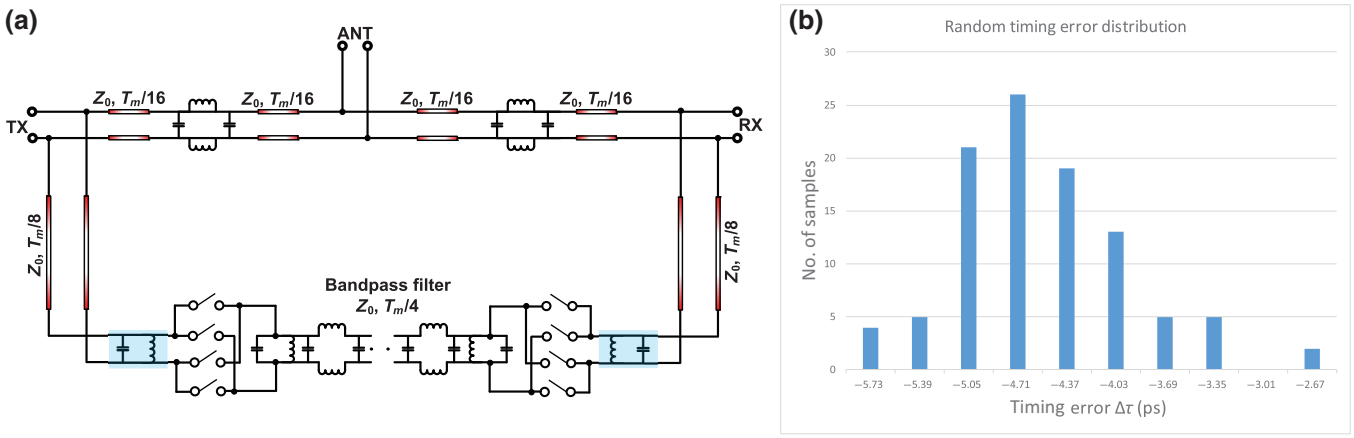

FIG. 21. (a) Circuit schematic of a realistic differential circulator manufactured on a 45-nm CMOS platform. (b) Distribution of the timing error in a realistic circuit. Total number of samples is 100. The average value of $\Delta\tau$ is -4.53 ps and the standard deviation of $\Delta\tau$ is 0.61 ps. As we increase the number of iterations, the distribution converges to a Gaussian distribution.

Random mismatch simulations of the clock path predict that the $\Delta\tau$ varies with a mean value of 4.53 ps, which results in 3.9% relative time delay [see Fig. 21(b)]. This leads to an extra insertion loss of 0.7 dB and nonideal isolation around 22 dB. These simulated loss and isolation variations agree well with our theoretical calculations [see Eq. (39)].

VI. CONCLUSIONS

In this work we present several nonreciprocal devices based on commutated switch networks and analyze the effects of switch desynchronization on their performance. Our main conclusion is that commutated switch networks provide an excellent platform to realize nonreciprocal devices, such as gyrators, isolators, and circulators, with excellent performance metrics. Timing errors in the switching schemes do not affect return loss in all these devices. In turn, insertion loss and isolation degrade linearly with an increase in timing error. In general, there is an upper bound for the timing error for the insertion loss and isolation to remain below certain thresholds, but these limits are readily achievable in conventional integrated circuit layouts. Furthermore, integrated-circuit implementations enable the design of calibration circuitry that corrects for timing errors, and our results provide guidelines for the nature and extent of the errors that should be calibrated. We find that for isolation larger than 20 dB and insertion loss smaller than 3 dB, the timing error should be smaller than 7.3, 5, 5% for the gyrator, isolator, and circulator, respectively. We present opportunities to realize very large (in principle infinite) isolation, circulation, and nonreciprocal phase shifts, and in some instances these bandwidths can be preserved even in the presence of timing errors by suitably controlling the switch resistance. In practice, there are more nonidealities that can be investigated in these systems, including dispersion in the delay-line sections, finite rise and fall times of the switches, and other desynchronization scenarios. These phenomena go beyond the scope of this work. Overall, our results show a positive outlook for commutated switching networks for nonreciprocal functionalities, given their direct integrability in a vast family of circuit technologies, and their very small footprint. We envision that similar concepts may be extended also to acoustics and photonics, opening exciting opportunities to broaden the family of efficient magnet-free nonreciprocal devices based on spatial-temporal modulation.

ACKNOWLEDGMENTS

This work is supported by the DARPA SPAR program, the NSF EFRI program, the Simons Foundation, and the AFOSR MURI program.

APPENDIX A. HARMONIC ANALYSIS OF GYRATORS

1. Singly balanced gyrator

For the upper branch gyrator, we assume that the input signal at port 1 of the singly balanced gyrator is monochromatic with $e^{j\omega t}$. Performing the Fourier transform of Eqs. (1) and (2) in the main text we obtain the reflected and transmitted signals

$$V_2^-(t) = \sum_{n=-\infty}^{n=+\infty} \frac{(-1)^n \sin\frac{n\pi}{2}}{n\pi} e^{-j\omega\frac{T_m}{4}} e^{j(\omega+n\omega_m)t}, \tag{A1}$$

$$V_1^-(t) = \sum_{n=-\infty}^{n=+\infty} \frac{e^{j\frac{n\pi}{2}} \sin\frac{n\pi}{2}}{n\pi} e^{j(\omega+n\omega_m)t}. \tag{A2}$$

Similarly, Fourier transforming Eqs. (3) and (4) in the main text we obtain the reflected and transmitted signals for excitation from port 2:

$$V_1^-(t) = \sum_{n=-\infty}^{n=+\infty} \frac{e^{-j\frac{n\pi}{2}} \sin\frac{n\pi}{2}}{n\pi} e^{-j\omega\frac{3T_m}{4}} e^{j(\omega+n\omega_m)t}, \tag{A3}$$

$$V_2^-(t) = \sum_{n=-\infty}^{n=+\infty} \frac{\sin\frac{n\pi}{2}}{n\pi} e^{j(\omega+n\omega_m)t}. \tag{A4}$$

We notice that all the scattering parameters of the fundamental tone are multiplied with a factor 1/2, leading to 6-dB insertion loss for the transmitted signal in both directions. There are two mechanisms contributing to this factor. First, the switches transmit only during half of the modulation period, whichever port is excited, allowing only half of the incident power to enter the device. Second, again due to the switches, in the reflected and transmitted signals, the total power distributed to all the higher-order harmonic is

$$\sum_{\substack{n=-\infty \\ n\neq 0}}^{+\infty} \frac{\sin^2\left(\frac{n\pi}{2}\right)}{n^2\pi^2} = \sum_{n=\pm1,\pm3,\pm5\cdots} \frac{1}{n^2\pi^2} = \frac{1}{4}, \tag{A5}$$

which is half of the power that gets into the circuit. Therefore, the power that gets out of the circuit at the fundamental tone is 1/4 of the input power, resulting in an insertion loss of 6 dB.

We continue to perform the harmonic analysis of a slightly desynchronized single-branch gyrator. To analyze the scattering properties, we transform Eqs. (9)–(12) to

Fourier series:

$$V_2^-(t) = \sum_{n\neq 0} \frac{j^{n+1}[1-(-1)^n e^{-jn\omega_m|\Delta\tau|}]}{2n\pi} e^{-j\omega\frac{T_m}{4}} e^{j(\omega+n\omega_m)t} + \left(\frac{1}{2} - \frac{|\Delta\tau|}{T_m}\right) e^{-j\omega\frac{T_m}{4}} e^{j\omega t} + \sum_{n\neq 0} \frac{j^{n+1}[-1+e^{-jn\omega_m|\Delta\tau|}]}{2n\pi} e^{-j\omega\frac{3T_m}{4}} e^{j(\omega+n\omega_m)t} + \frac{|\Delta\tau|}{T_m} e^{-j\omega\frac{3T_m}{4}} e^{j\omega t}, \tag{A6}$$

$$V_1^-(t) = \sum_{n=-\infty}^{n=+\infty} \frac{e^{j\frac{n\pi}{2}} \sin\frac{n\pi}{2}}{n\pi} e^{j(\omega+n\omega_m)t}, \tag{A7}$$

$$V_1^-(t) = \sum_{n\neq 0} \frac{j[(-1)^n - e^{-jn\omega_m|\Delta\tau|}]}{2n\pi} e^{-j\omega\frac{3T_m}{4}} e^{j(\omega+n\omega_m)t} + \left(\frac{1}{2} - \frac{|\Delta\tau|}{T_m}\right) e^{-j\omega\frac{3T_m}{4}} e^{j\omega t} + \sum_{n\neq 0} \frac{j[-1+e^{-jn\omega_m|\Delta\tau|}]}{2n\pi} e^{-j\omega\frac{T_m}{4}} e^{j(\omega+n\omega_m)t} + \frac{|\Delta\tau|}{T_m} e^{-j\omega\frac{T_m}{4}} e^{j\omega t}, \tag{A8}$$

$$V_2^-(t) = \sum_{n=-\infty}^{n=+\infty} \frac{\sin\frac{n\pi}{2}}{n\pi} e^{j(\omega+n\omega_m)t} e^{-jn\omega_m|\Delta\tau|}. \tag{A9}$$

The above equations reduce to Eqs. (A1)–(A4) when timing error $\Delta\tau$ is set to zero. When the second switch is desynchronized, the transmitted signals possess both odd and even harmonics rather than odd harmonics only as in the perfect synchronization case.

The harmonic analyses of a double-branch gyrator with timing error are again given by

$$V_2^-(t) = \sum_{n\neq 0} \frac{j\cos\frac{n\pi}{2}[1-e^{-jn\omega_m|\Delta\tau|}]}{n\pi} \left(e^{-j\omega\frac{T_m}{4}} - e^{-j\omega\frac{3T_m}{4}}\right) \times e^{j(\omega+n\omega_m)t} + \left[\left(1-\frac{2|\Delta\tau|}{T_m}\right) e^{-j\omega\frac{T_m}{4}} + \frac{2|\Delta\tau|}{T_m} e^{-j\omega\frac{3T_m}{4}}\right] e^{j\omega t}, \tag{A10}$$

$$V_1^-(t) = 0, \tag{A11}$$

$$V_1^-(t) = \sum_{n\neq 0} \frac{j[(-1)^n+1][1-e^{-jn\omega_m|\Delta\tau|}]}{2n\pi} \times \left(e^{-j\omega\frac{3T_m}{4}} - e^{-j\omega\frac{T_m}{4}}\right) e^{j(\omega+n\omega_m)t} + \left[\left(1-\frac{2|\Delta\tau|}{T_m}\right) e^{-j\omega\frac{3T_m}{4}} + \frac{2|\Delta\tau|}{T_m} e^{-j\omega\frac{T_m}{4}}\right] e^{j\omega t}, \tag{A12}$$

$$V_2^-(t) = 0. \tag{A13}$$

The above equations indicate that the double-branch gyrator has residual even-order harmonics in the presence of the desynchronization.

2. Differential gyrator

To study the IM products and scattering properties of the fundamental tone, we perform a Fourier transform over the temporal response and get the Fourier series of the responses:

$$V_2^-(t) = \sum_{n\neq 0} \frac{2j\ \cos\frac{n\pi}{2}[1-e^{-jn\omega_m|\Delta\tau|}]}{n\pi} e^{j(\omega+n\omega_m)t} e^{-j\omega\frac{T_m}{4}} + \left(1-\frac{4|\Delta\tau|}{T_m}\right) e^{-j\omega\frac{T_m}{4}} e^{j\omega t}, \tag{A14}$$

$$V_1^-(t) = 0, \tag{A15}$$

$$V_1^-(t) = \sum_{n\neq 0} \frac{-j[1+(-1)^n][1-e^{-jn\omega_m|\Delta\tau|}]}{n\pi} e^{j(\omega+n\omega_m)t} \times e^{-j\omega\frac{T_m}{4}} - \left(1-\frac{4|\Delta\tau|}{T_m}\right) e^{-j\omega\frac{T_m}{4}} e^{j\omega t}, \tag{A16}$$

$$V_2^-(t) = 0. \tag{A17}$$

The above equation demonstrates the same IM products as Eqs. (A10)–(A13). Therefore, they share the identical IM products distribution as shown in Fig. 4.

APPENDIX B. TEMPORAL AND SPECTRAL ANALYSIS OF ISOLATORS

1. Singly balanced isolator

For a single-branch isolator, the temporal domain responses are expressed in Eqs. (25)–(28). The Fourier

series can be easily obtained:

$$V_2^-(t) = \sum_{n=-\infty}^{n=+\infty} \frac{\sin\frac{n\pi}{2}}{n\pi}[(-1)^n + T^2]e^{-j\omega\frac{T_m}{4}}e^{j(\omega+n\omega_m)t}, \tag{B1}$$

$$V_1^-(t) = \sum_{n=-\infty}^{n=+\infty} \frac{\Gamma\left(e^{j\frac{n\pi}{2}} + Te^{-j\frac{n\pi}{2}}e^{-j\omega\frac{T_m}{2}}\right)\sin\frac{n\pi}{2}}{n\pi}e^{j(\omega+n\omega_m)t}, \tag{B2}$$

$$V_1^-(t) = Te^{-j\omega\frac{T_m}{4}}e^{j\omega t} + \sum_{n=-\infty}^{n=+\infty} \frac{\Gamma^2 e^{-j\frac{n\pi}{2}}\sin\frac{n\pi}{2}}{n\pi} \times e^{-j\omega\frac{3T_m}{4}}e^{j(\omega+n\omega_m)t}, \tag{B3}$$

$$V_2^-(t) = \sum_{n=-\infty}^{n=+\infty} \Gamma\left[1 + Te^{-j\omega\frac{T_m}{2}}\right]\frac{\sin\frac{n\pi}{2}}{n\pi}e^{j(\omega+n\omega_m)t}. \tag{B4}$$

For a singly balanced isolator, the analysis is much more complicated. Assume that the network is excited with a monochromatic signal $V_1^+(t) = \exp(j\omega t)$ at port 1. The left side of the network is essentially a Wye-topology network with time-varying scattering properties $S(t)$. The output and input signals obey the following relation:

$$\begin{bmatrix} V_1^-(t) \\ V_a^+(t) \\ V_b^+(t) \end{bmatrix} = S(t)\begin{bmatrix} V_1^+(t) \\ V_a^-(t) \\ V_b^-(t) \end{bmatrix}, \tag{B5}$$

where the time-domain scattering matrix is

$$S(t) = \begin{bmatrix} \frac{R}{3R+8} & \frac{4}{3R+8} + \frac{2R}{3R+8}P_1(t) & \frac{2R+4}{3R+8} + \frac{-2R}{3R+8}P_1(t) \\ \frac{8}{3R+8} + \frac{4R}{3R+8}P_1(t) & \frac{3R-4}{3R+8} - \frac{4R}{3R+8}P_1(t) & \frac{4}{3R+8} \\ \frac{4R+8}{3R+8} - \frac{4R}{3R+8}P_1(t) & \frac{4}{3R+8} & \frac{-R-4}{3R+8} + \frac{4R}{3R+8}P_1(t) \end{bmatrix}, \tag{B6}$$

and $R = R_m/Z_0$ is the relative resistance. Meanwhile, the right side of the network is also a Wye-topology network with the following scattering relations:

$$\begin{bmatrix} V_2^-(t) \\ V_a^-\left(t+\frac{T_m}{4}\right) \\ V_b^-\left(t+\frac{T_m}{4}\right) \end{bmatrix} = S\left(t-\frac{T_m}{4}\right)\begin{bmatrix} 0 \\ V_a^+\left(t-\frac{T_m}{4}\right) \\ V_b^+\left(t-\frac{T_m}{4}\right) \end{bmatrix}. \tag{B7}$$

From Eqs. (B5) and (B7), we have the following relations:

$$\begin{cases} V_a^+(t) = S_{21}V_1^+(t) + S_{22}V_a^-(t) + S_{23}V_b^-(t), \\ V_b^+(t) = S_{31}V_1^+(t) + S_{32}V_a^-(t) + S_{33}V_b^-(t), \end{cases} \tag{B8}$$

and

$$\begin{cases} V_a^-\left(t+\frac{T_m}{2}\right) = S_{22}V_a^+(t) + S_{23}V_b^+(t), \\ V_b^-\left(t+\frac{T_m}{2}\right) = S_{32}V_a^+(t) + S_{33}V_b^+(t). \end{cases} \tag{B9}$$

We substitute Eq. (B8) into Eq. (B9) and get

$$\begin{cases} V_a^-\left(t+\frac{T_m}{2}\right) = S_{22}[S_{21}V_1^+(t) + S_{22}V_a^-(t) + S_{23}V_b^-(t)] + S_{23}[S_{31}V_1^+(t) + S_{32}V_a^-(t) + S_{33}V_b^-(t)], \\ V_b^-\left(t+\frac{T_m}{2}\right) = S_{32}[S_{21}V_1^+(t) + S_{22}V_a^-(t) + S_{23}V_b^-(t)] + S_{33}[S_{31}V_1^+(t) + S_{32}V_a^-(t) + S_{33}V_b^-(t)]. \end{cases} \tag{B10}$$

Shifting the reference time of the above equation by $T_m/2$ and employing the Bloch theorem

$$\begin{cases} V_a^-(t+T_m) = V_a^-(t)\exp(j\omega T_m), \\ V_b^-(t+T_m) = V_b^-(t)\exp(j\omega T_m), \end{cases} \tag{B11}$$

we obtain the following linear equations for V_a^- and V_b^-:

$$\begin{cases} V_a^-(t)\exp(j\omega T_m) &= \left[S_{22}\left(t+\frac{T_m}{2}\right)S_{21}\left(t+\frac{T_m}{2}\right)+S_{23}\left(t+\frac{T_m}{2}\right)S_{31}\left(t+\frac{T_m}{2}\right)\right]V_1^+\left(t+\frac{T_m}{2}\right) \\ &\quad +\left[S_{22}\left(t+\frac{T_m}{2}\right)S_{22}\left(t+\frac{T_m}{2}\right)+S_{23}\left(t+\frac{T_m}{2}\right)S_{32}\left(t+\frac{T_m}{2}\right)\right] \\ &\quad \times[(S_{22}S_{21}+S_{23}S_{31})V_1^+(t)+(S_{22}S_{22}+S_{23}S_{32})V_a^-(t)+(S_{22}S_{23}+S_{23}S_{33})V_b^-(t)] \\ &\quad +\left[S_{22}\left(t+\frac{T_m}{2}\right)S_{23}\left(t+\frac{T_m}{2}\right)+S_{23}\left(t+\frac{T_m}{2}\right)S_{33}\left(t+\frac{T_m}{2}\right)\right] \\ &\quad \times[(S_{32}S_{21}+S_{33}S_{31})V_1^+(t)+(S_{32}S_{22}+S_{33}S_{32})V_a^-(t)+(S_{32}S_{23}+S_{33}S_{33})V_b^-(t)], \\ V_b^-(t)\exp(j\omega T_m) &= \left[S_{32}\left(t+\frac{T_m}{2}\right)S_{21}\left(t+\frac{T_m}{2}\right)+S_{33}\left(t+\frac{T_m}{2}\right)S_{31}\left(t+\frac{T_m}{2}\right)\right]V_1^+\left(t+\frac{T_m}{2}\right) \\ &\quad +\left[S_{32}\left(t+\frac{T_m}{2}\right)S_{22}\left(t+\frac{T_m}{2}\right)+S_{33}\left(t+\frac{T_m}{2}\right)S_{32}\left(t+\frac{T_m}{2}\right)\right] \\ &\quad \times[(S_{22}S_{21}+S_{23}S_{31})V_1^+(t)+(S_{22}S_{22}+S_{23}S_{32})V_a^-(t)+(S_{22}S_{23}+S_{23}S_{33})V_b^-(t)] \\ &\quad +\left[S_{32}\left(t+\frac{T_m}{2}\right)S_{23}\left(t+\frac{T_m}{2}\right)+S_{33}\left(t+\frac{T_m}{2}\right)S_{33}\left(t+\frac{T_m}{2}\right)\right] \\ &\quad \times[(S_{32}S_{21}+S_{33}S_{31})V_1^+(t)+(S_{32}S_{22}+S_{33}S_{32})V_a^-(t)+(S_{32}S_{23}+S_{33}S_{33})V_b^-(t)]. \end{cases} \tag{B12}$$

We solve the linear Eqs. (B8) and (B12) together and get the solutions of V_a^+, V_b^+, V_a^-, V_b^-. Then, the reflected signals and transmitted signals can be expressed as a linear combination of the above known signals

$$\begin{cases} V_1^-(t) = S_{11}(t)+S_{12}(t)V_a^-(t)+S_{13}(t)V_b^-, \\ V_2^-(t) = [S_{12}(t)V_a^+(t)+S_{13}(t)V_b^+]e^{-j\omega\frac{T_m}{4}}. \end{cases} \tag{B13}$$

The frequency-domain scattering parameters of the fundamental tone is essentially the time-average value of the envelope of the above equation, which can be easily obtained

$$\begin{aligned} \mathscr{S}_{11}(\omega) &= \frac{\left(1+e^{j\omega\frac{T_m}{2}}\right)R\left[8-3R+e^{j\omega\frac{T_m}{2}}(8+3R)\right]}{-16e^{j\omega\frac{T_m}{2}}(-4+R)-R^2+e^{j\omega T_m}(8+3R)^2}, \\ \mathscr{S}_{21}(\omega) &= \frac{8e^{j\omega\frac{T_m}{4}}\left[8-4R+4e^{j\omega\frac{T_m}{2}}(R^2+4R+8)\right]}{-16e^{j\omega\frac{T_m}{2}}(-4+R)-R^2+e^{j\omega T_m}(8+3R)^2}. \end{aligned} \tag{B14}$$

We follow the same procedures for excitation at port 2 and figure out the scattering parameters

$$\begin{aligned} \mathscr{S}_{22}(\omega) &= \frac{\left(1+e^{j\omega\frac{T_m}{2}}\right)R\left[8-3R+e^{j\omega\frac{T_m}{2}}(8+3R)\right]}{-16e^{j\omega\frac{T_m}{2}}(-4+R)-R^2+e^{j\omega T_m}(8+3R)^2}, \\ \mathscr{S}_{12}(\omega) &= \frac{8e^{j\omega\frac{T_m}{4}}\left[8+(-4+R)R+4e^{j\omega\frac{T_m}{2}}(2+R)\right]}{-16e^{j\omega\frac{T_m}{2}}(-4+R)-R^2+e^{j\omega T_m}(8+3R)^2}. \end{aligned} \tag{B15}$$

Equations (B14) and (B15) are the major results of this section. They will degenerate to Eq. (33) in the main text at operational frequency $\omega = (2k+1)\omega_m, k = 0, 1, 2, 3\cdots$.

2. Synchronization analysis of a single-branch isolator

In this appendix, we perform a rigorous time and frequency analysis of a single-branch isolator with timing error. Assume that port 1 is excited with a monochromatic signal $\exp(j\omega t)$. In the first half modulation period, most of the signal passes through the second switch with time delay $T_m/4$, apart from a small tail that experiences partial transmission through port 2. The mismatched tail is partially

reflected at port 2 and bounces back to port 1 with another partial reflection at port 1. The partially reflected signal is transmitted through the transmission line again and fully transports through the second switch. In the second half modulation period, a small tail experiences partial transmission through port 1 and fully transmits through port 2 due to time mismatch. However, most of the signal during this modulation period is partially transmitted through switch 1 and switch 2 with transmission coefficient T^2. The reflected signal at port 1 can be analyzed in a similar way, and we summarize the responses for excitation from port 1 below:

$$\begin{cases} V_2^-(t) = V_1^+\left(t-\frac{T_m}{4}\right)\left[\xi_1(t)+T\xi_2(t)+T\xi_2\left(t-\frac{T_m}{2}\right)\right]+\Gamma^2 V_1^+\left(t-\frac{3T_m}{4}\right)\xi_2\left(t-\frac{T_m}{2}\right) \\ \qquad\quad +T^2 V_1^+\left(t-\frac{3T_m}{4}\right)\xi_1\left(t-\frac{T_m}{2}\right), \\ V_1^-(t) = \Gamma T V_1^+\left(t-\frac{T_m}{2}\right)\xi_2\left(t-\frac{T_m}{4}\right)+\Gamma V_1^+(t)[1-P_1(t)]+\Gamma T V_1^+\left(t-\frac{T_m}{2}\right)\xi_1\left(t-\frac{3T_m}{4}\right), \end{cases} \tag{B16}$$

where $\xi_1(t)$ and $\xi_2(t)$ are envelopes of the modulated signal [see Fig. 22], $V_2^-(t)$ is the transmitted signal, and $V_1^-(t)$ is the reflected signal at port 1. The above temporal responses at port 1 can be analyzed to a Fourier series as

$$\begin{cases} V_2^-(t) = \sum_{n\neq 0}\frac{j^{n+1}(1-\mathrm{T})[1-(-1)^n\mathrm{T}][1-(-1)^n e^{-jn\omega|\Delta\tau|}]}{2n\pi}e^{-j\omega\frac{T_m}{4}}e^{j(\omega+n\omega_m)t} \\ \qquad\quad +\sum_{n\neq 0}\Gamma^2\frac{j^{n+1}}{2n\pi}(-1+e^{-jn\omega|\Delta\tau|})e^{-j\omega\frac{3T_m}{4}}e^{j(\omega+n\omega_m)t}+\Gamma^2\frac{|\Delta\tau|}{T_m}e^{-j\omega\frac{3T_m}{4}}e^{j\omega t}, \\ V_1^-(t) = \sum_{n\neq 0}\frac{j[-1+(-1)^n]e^{-jn\omega|\Delta\tau|}}{2n\pi}\Gamma\mathrm{T}e^{-j\omega\frac{T_m}{2}}e^{j(\omega+n\omega_m)t}+\frac{\Gamma\mathrm{T}}{2}e^{-j\omega\frac{T_m}{2}}e^{j\omega t}+\sum_{n\neq 0}\frac{j\Gamma[1-(-1)^n]}{2n\pi}e^{j(\omega+n\omega_m)t}+\frac{\Gamma}{2}e^{j\omega t}. \end{cases} \tag{B17}$$

For monochromatic excitation $\exp(j\omega t)$ at port 2, most of the signal is fully transmitted through switch 2 and partially transmitted through switch 1. The reflected signal bounces back and forth and transmits through switch 1 with an amplitude Γ^2. In the first half modulation period, a small desynchronized tail passes through switch 1 without

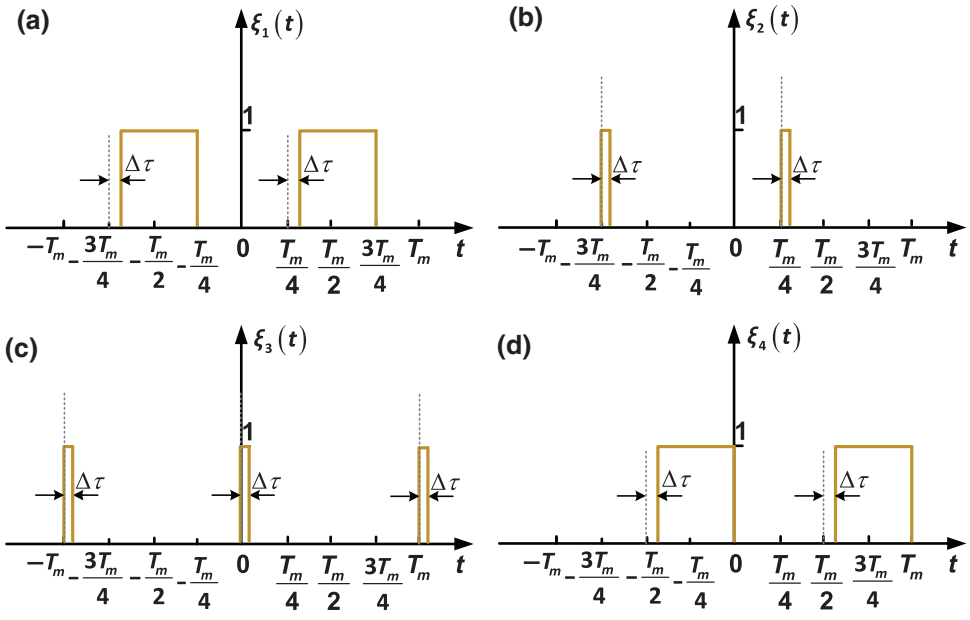

FIG. 22. Envelope of modulated signals of a single-branch isolator with timing error. (a) Forward transmitted signal envelope from excitation at port 1; (b) forward transmitted signal envelope tail from excitation at port 1; (c) backward transmitted signal envelope tail from excitation at port 2; (d) backward transmitted signal envelope from excitation at port 2.

loss. In the second half modulation period, most of the signal is partially transmitted through switch 2 with amplitude T, and then fully transmitted through switch 1. A small tail partially transmits through switch 2 and then partially transmits through switch 1, with an amplitude T^2. The reflected signal at port 2 can be analyzed in a similar way, and we summarize the responses for excitation from port 2 below:

$$\begin{cases} V_1^-(t) = V_2^+\left(t-\frac{T_m}{4}\right)\left[\xi_3(t)+T\xi_4(t)+T\xi_4\left(t-\frac{T_m}{2}\right)\right]+\Gamma^2 V_2^+\left(t-\frac{3T_m}{4}\right)\xi_4\left(t-\frac{T_m}{2}\right) \\ \qquad\qquad +T^2V_2^+\left(t-\frac{T_m}{4}\right)\xi_3\left(t-\frac{T_m}{2}\right), \\ V_2^-(t) = \Gamma T V_2^+\left(t-\frac{T_m}{2}\right)P_2(t)+\Gamma V_2^+(t)[1-P_2(t-|\Delta\tau|)], \end{cases} \tag{B18}$$

where $\xi_3(t)$ and $\xi_4(t)$ are envelopes of modulated signal [see Fig. 22], $V_1^-(t)$ is transmitted signal, and $V_2^-(t)$ is the reflected signal at port 1. The above temporal responses can be expressed in frequency domain as

$$\begin{cases} V_1^-(t) = \sum_{n\neq 0}\frac{j(1-T)[1-(-1)^nT](-1+e^{-jn\omega|\Delta\tau|})}{2n\pi}e^{-j\omega\frac{T_m}{4}}e^{j(\omega+n\omega_m)t}+\left(T+\Gamma^2\frac{|\Delta\tau|}{T_m}\right)e^{-j\omega\frac{T_m}{4}}e^{j\omega t} \\ \qquad \sum_{n\neq 0}\frac{j\Gamma^2}{2n\pi}[(-1)^n-e^{-jn\omega|\Delta\tau|}]e^{-j\omega\frac{3T_m}{4}}e^{j(\omega+n\omega_m)t}+\frac{\Gamma^2}{2}\left(1-\frac{2|\Delta\tau|}{T_m}\right)e^{-j\omega\frac{3T_m}{4}}e^{j\omega t}, \\ V_2^-(t) = \sum\frac{\Gamma\sin\frac{n\pi}{2}}{n\pi}\left(e^{-jn\omega|\Delta\tau|}+Te^{-j\omega\frac{T_m}{2}}\right)e^{j(\omega+n\omega_m)t}+\frac{\Gamma T}{2}e^{-j\omega\frac{T_m}{2}}e^{j\omega t}+\frac{\Gamma}{2}e^{j\omega t}. \end{cases} \tag{B19}$$

In summary, we analyze the temporal as well as frequency responses of a desynchronized single-branch isolator. Equations (B17) and (B19) are our major results and they become Eqs. (B1)–(B4) when the timing error is zero.

3. Ultrabroad-band isolator

When there is timing error in the ultrabroad-band isolator, we transform the time-domain responses into Fourier series:

$$V_2^-(t) = \sum_{n\neq 0}\frac{j\cos\frac{n\pi}{2}[1-e^{-jn\omega_m|\Delta\tau|}]}{n\pi}e^{j(\omega+n\omega_m)t}e^{-j\omega\frac{T_m}{4}} + \left(1-\frac{2|\Delta\tau|}{T_m}\right)e^{-j\omega\frac{T_m}{4}}e^{j\omega t}, \tag{B20}$$

$$V_1^-(t) = 0, \tag{B21}$$

$$V_1^-(t) = \sum_{n\neq 0}\frac{-j[1+(-1)^n][1-e^{-jn\omega_m|\Delta\tau|}]}{2n\pi}e^{j(\omega+n\omega_m)t} \times e^{-j\omega\frac{T_m}{4}}+\frac{2|\Delta\tau|}{T_m}e^{-j\omega\frac{T_m}{4}}e^{j\omega t}, \tag{B22}$$

$$V_2^-(t) = 0. \tag{B23}$$

From the above equations, we can infer that the both forward and backward propagation signal share the same IM products distribution, which is enveloped by a sinc function: $2|\Delta\tau|/T_m\mathrm{sinc}(n\pi|\Delta\tau|/T_m)$. Figure 14 demonstrates the IM products of this isolator with relative timing error $|\Delta\tau|/T_m = 0.1$. The fundamental tone of the forward transmission signal is 0.8, while the fundamental of the backward transmission signal is 0.2.

APPENDIX C. ANALYSIS OF CIRCULATORS

1. Singly balanced circulator

In this appendix, we present a rigorous temporal and frequency domain analysis of the singly balanced circulator. Assume that the network is excited with a monochromatic signal $V_1^+(t) = \exp(j\omega t)$ at port 1. Then, we have the following relation:

$$\begin{bmatrix} V_1^-(t) \\ V_b^+(t) \\ V_a^+(t) \end{bmatrix} = S(t)\begin{bmatrix} V_1^+(t) \\ V_b^-(t) \\ V_a^-(t-T_m/2) \end{bmatrix}, \tag{C1}$$

Where the time-domain scattering parameter is

$$S(t) = \begin{bmatrix} -\frac{1}{3} & \frac{2}{3} & \frac{2}{3} \\ \frac{2}{3} & -\frac{1}{3} & \frac{2}{3} \\ \frac{2}{3} & \frac{2}{3} & -\frac{1}{3} \end{bmatrix}. \tag{C2}$$

Meanwhile, at port 2 we have

$$\begin{bmatrix} V_2^-(t) \\ V_c^+(t) \\ V_a^-(t) \end{bmatrix} = S(t) \begin{bmatrix} 0 \\ V_c^-(t) \\ V_a^+(t - T_m) \end{bmatrix}. \tag{C3}$$

At port 3, we have

$$\begin{bmatrix} V_3^-(t) \\ V_b^-\left(t + \frac{T_m}{4}\right) \\ V_c^-\left(t + \frac{T_m}{4}\right) \end{bmatrix} = S(t) \begin{bmatrix} 0 \\ V_b^+\left(t - \frac{T_m}{4}\right) \\ V_c^+\left(t - \frac{T_m}{4}\right) \end{bmatrix}. \tag{C4}$$

Since the scattering parameters are time independent, we can perform a Fourier transform over Eqs. (C1), (C3), and (C4). The matrix form of these equations is

$$\begin{bmatrix} 0 & -1 & 0 & S_{23}e^{-j\omega\frac{T_m}{2}} & S_{22} & 0 \\ -1 & 0 & 0 & S_{33}e^{-j\omega\frac{T_m}{2}} & S_{32} & 0 \\ 0 & S_{22}e^{-j\omega\frac{T_m}{2}} & S_{23}e^{-j\omega\frac{T_m}{2}} & 0 & -1 & 0 \\ 0 & S_{32}e^{-j\omega\frac{T_m}{2}} & S_{33}e^{-j\omega\frac{T_m}{2}} & 0 & 0 & -1 \\ S_{23}e^{-j\omega T_m} & 0 & -1 & 0 & 0 & S_{22} \\ S_{33}e^{-j\omega T_m} & 0 & 0 & -1 & 0 & S_{32} \end{bmatrix} \begin{bmatrix} V_a^+(\omega) \\ V_b^+(\omega) \\ V_c^+(\omega) \\ V_a^-(\omega) \\ V_b^-(\omega) \\ V_c^-(\omega) \end{bmatrix} = \begin{bmatrix} -S_{21}V_1^+(\omega) \\ -S_{31}V_1^+(\omega) \\ 0 \\ 0 \\ 0 \\ 0 \end{bmatrix}. \tag{C5}$$

We solve the above linear equation, substitute the solution into (C1), (C3), and (C4), and get the scattering parameters

$$\begin{cases} \mathscr{S}_{11}(\omega) = -\dfrac{2 + 5\cos\left(\frac{\pi\omega}{\omega_m}\right) + 3\cos\left(\frac{2\pi\omega}{\omega_m}\right) + j\,6\sin\left(\frac{\pi\omega}{\omega_m}\right) + j\,6\sin\left(\frac{2\pi\omega}{\omega_m}\right)}{6 + 11\cos\left(\frac{\pi\omega}{\omega_m}\right) + 13\cos\left(\frac{2\pi\omega}{\omega_m}\right) + j\,10\sin\left(\frac{\pi\omega}{\omega_m}\right) + j\,14\sin\left(\frac{2\pi\omega}{\omega_m}\right)}, \\ \mathscr{S}_{21}(\omega) = -\dfrac{2\left[5 + 5\cos\left(\frac{\pi\omega}{\omega_m}\right) - j\,\sin\left(\frac{\pi\omega}{\omega_m}\right)\right]}{6 + 11\cos\left(\frac{\pi\omega}{\omega_m}\right) + 13\cos\left(\frac{2\pi\omega}{\omega_m}\right) + j\,10\sin\left(\frac{\pi\omega}{\omega_m}\right) + j\,14\sin\left(\frac{2\pi\omega}{\omega_m}\right)}, \\ \mathscr{S}_{31}(\omega) = \dfrac{4\left[3\cos\left(\frac{\pi\omega}{2\omega_m}\right) + 2\cos\left(\frac{3\pi\omega}{2\omega_m}\right) - j\,\sin\left(\frac{\pi\omega}{2\omega_m}\right) + j\,\sin\left(\frac{3\pi\omega}{2\omega_m}\right)\right]}{6 + 11\cos\left(\frac{\pi\omega}{\omega_m}\right) + 13\cos\left(\frac{2\pi\omega}{\omega_m}\right) + j\,10\sin\left(\frac{\pi\omega}{\omega_m}\right) + j\,14\sin\left(\frac{2\pi\omega}{\omega_m}\right)}. \end{cases} \tag{C6}$$

We execute similar analyses at port 2 and port 3 and get the scattering parameters

$$\begin{cases} \mathscr{S}_{12}(\omega) = -\dfrac{2\left[3 + 7\cos\left(\frac{\pi\omega}{\omega_m}\right) + j\,3\sin\left(\frac{\pi\omega}{\omega_m}\right)\right]}{6 + 11\cos\left(\frac{\pi\omega}{\omega_m}\right) + 13\cos\left(\frac{2\pi\omega}{\omega_m}\right) + j\,10\sin\left(\frac{\pi\omega}{\omega_m}\right) + j\,14\sin\left(\frac{2\pi\omega}{\omega_m}\right)}, \\ \mathscr{S}_{22}(\omega) = -\dfrac{2 + 5\cos\left(\frac{\pi\omega}{\omega_m}\right) + 3\cos\left(\frac{2\pi\omega}{\omega_m}\right) + j\,6\sin\left(\frac{\pi\omega}{\omega_m}\right) + j\,6\sin\left(\frac{2\pi\omega}{\omega_m}\right)}{6 + 11\cos\left(\frac{\pi\omega}{\omega_m}\right) + 13\cos\left(\frac{2\pi\omega}{\omega_m}\right) + j\,10\sin\left(\frac{\pi\omega}{\omega_m}\right) + j\,14\sin\left(\frac{2\pi\omega}{\omega_m}\right)}, \\ \mathscr{S}_{32}(\omega) = \dfrac{4\cos\left(\frac{\pi\omega}{2\omega_m}\right)\left[1 + 4\cos\left(\frac{\pi\omega}{\omega_m}\right) + j\,2\sin\left(\frac{\pi\omega}{\omega_m}\right)\right]}{6 + 11\cos\left(\frac{\pi\omega}{\omega_m}\right) + 13\cos\left(\frac{2\pi\omega}{\omega_m}\right) + j\,10\sin\left(\frac{\pi\omega}{\omega_m}\right) + j\,14\sin\left(\frac{2\pi\omega}{\omega_m}\right)}. \end{cases} \tag{C7}$$

and

$$\begin{cases} \mathscr{S}_{13}(\omega) = \dfrac{4\cos\left(\frac{\pi\omega}{2\omega_m}\right)\left[1+4\cos\left(\frac{\pi\omega}{\omega_m}\right)+j\,2\sin\left(\frac{\pi\omega}{\omega_m}\right)\right]}{6+11\cos\left(\frac{\pi\omega}{\omega_m}\right)+13\cos\left(\frac{2\pi\omega}{\omega_m}\right)+j\,10\sin\left(\frac{\pi\omega}{\omega_m}\right)+j\,14\sin\left(\frac{2\pi\omega}{\omega_m}\right)}, \\ \mathscr{S}_{23}(\omega) = \dfrac{4\left[3\cos\left(\frac{\pi\omega}{2\omega_m}\right)+2\cos\left(\frac{3\pi\omega}{2\omega_m}\right)-j\,\sin\left(\frac{\pi\omega}{2\omega_m}\right)+j\,\sin\left(\frac{3\pi\omega}{2\omega_m}\right)\right]}{6+11\cos\left(\frac{\pi\omega}{\omega_m}\right)+13\cos\left(\frac{2\pi\omega}{\omega_m}\right)+j\,10\sin\left(\frac{\pi\omega}{\omega_m}\right)+j\,14\sin\left(\frac{2\pi\omega}{\omega_m}\right)}, \\ \mathscr{S}_{33}(\omega) = -\dfrac{2+5\cos\left(\frac{\pi\omega}{\omega_m}\right)+3\cos\left(\frac{2\pi\omega}{\omega_m}\right)+j\,10\sin\left(\frac{\pi\omega}{\omega_m}\right)+j\,6\sin\left(\frac{2\pi\omega}{\omega_m}\right)}{6+11\cos\left(\frac{\pi\omega}{\omega_m}\right)+13\cos\left(\frac{2\pi\omega}{\omega_m}\right)+j\,10\sin\left(\frac{\pi\omega}{\omega_m}\right)+j\,14\sin\left(\frac{2\pi\omega}{\omega_m}\right)}. \end{cases} \tag{C8}$$

Equations (C6)–(C8) are the major results of this section. They transform into Eq. (37) at operational frequency $\omega = (2k+1)\omega_m$, $k = 0,\ 1,\ 2,\ 3\ldots$.

2. Doubly balanced circulator

In this appendix, we present a rigorous temporal and frequency domain analysis of the doubly balanced circulator. Assume that the network is excited with a monochromatic signal $V_1^+(t) = \exp(j\,\omega t)$ at port 1. Then, we have the following relation:

$$\begin{bmatrix} V_1^-(t) \\ V_b^+(t) \\ V_a^+(t) \end{bmatrix} = S(t) \begin{bmatrix} V_1^+(t) \\ V_b^-(t) \\ V_a^-(t - T_m/2) \end{bmatrix}, \tag{C9}$$

Where the time-domain scattering parameter is

$$S(t) = \begin{bmatrix} -\frac{1}{3} & \frac{2}{3} & \frac{2}{3} \\ \frac{2}{3} & -\frac{1}{3} & \frac{2}{3} \\ \frac{2}{3} & \frac{2}{3} & -\frac{1}{3} \end{bmatrix}. \tag{C10}$$

Meanwhile, at port 2 we have

$$\begin{bmatrix} V_2^-(t) \\ V_c^+(t) \\ V_a^-(t) \end{bmatrix} = S(t) \begin{bmatrix} 0 \\ V_c^-(t) \\ -V_a^+\left(t - \dfrac{T_m}{2}\right) \end{bmatrix}. \tag{C11}$$

At port 3, we have

$$\begin{bmatrix} V_3^-(t) \\ V_b^-\left(t + \dfrac{T_m}{4}\right) \\ V_c^-\left(t + \dfrac{T_m}{4}\right) \end{bmatrix} = S(t) \begin{bmatrix} 0 \\ V_b^+\left(t - \dfrac{T_m}{4}\right) \\ V_c^+\left(t - \dfrac{T_m}{4}\right) \end{bmatrix}. \tag{C12}$$

Since the scattering parameters are time independent, we can perform a Fourier transform over Eqs. (C9), (C11), and (C12). The matrix form of these equations is

$$\begin{bmatrix} 0 & -1 & 0 & S_{23}e^{-j\omega\frac{T_m}{2}} & S_{22} & 0 \\ -1 & 0 & 0 & S_{33}e^{-j\omega\frac{T_m}{2}} & S_{32} & 0 \\ 0 & S_{22}e^{-j\omega\frac{T_m}{2}} & S_{23}e^{-j\omega\frac{T_m}{2}} & 0 & -1 & 0 \\ 0 & S_{32}e^{-j\omega\frac{T_m}{2}} & S_{33}e^{-j\omega\frac{T_m}{2}} & 0 & 0 & -1 \\ -S_{23}e^{-j\omega\frac{T_m}{4}} & 0 & -1 & 0 & 0 & S_{22} \\ -S_{33}e^{-j\omega\frac{T_m}{4}} & 0 & 0 & -1 & 0 & S_{32} \end{bmatrix} \begin{bmatrix} V_a^+(\omega) \\ V_b^+(\omega) \\ V_c^+(\omega) \\ V_a^-(\omega) \\ V_b^-(\omega) \\ V_c^-(\omega) \end{bmatrix} = \begin{bmatrix} -S_{21}V_1^+(\omega) \\ -S_{31}V_1^+(\omega) \\ 0 \\ 0 \\ 0 \\ 0 \end{bmatrix}. \tag{C13}$$

We solve the above linear equation, substitute the solution into (C9), (C11), and (C12), and get the scattering parameters

$$\begin{cases} \mathscr{S}_{11}(\omega) = \dfrac{1-2\cos\left(\frac{\pi\omega}{\omega_m}\right)-3\cos\left(\frac{2\pi\omega}{\omega_m}\right)-j\,6\sin\left(\frac{2\pi\omega}{\omega_m}\right)}{1-2\cos\left(\frac{\pi\omega}{\omega_m}\right)+13\cos\left(\frac{2\pi\omega}{\omega_m}\right)-j\,4\sin\left(\frac{\pi\omega}{\omega_m}\right)+j\,14\sin\left(\frac{2\pi\omega}{\omega_m}\right)}, \\ \mathscr{S}_{21}(\omega) = \dfrac{4\left[1+\cos\left(\frac{\pi\omega}{\omega_m}\right)-2j\,\sin\left(\frac{\pi\omega}{\omega_m}\right)\right]}{1-2\cos\left(\frac{\pi\omega}{\omega_m}\right)+13\cos\left(\frac{2\pi\omega}{\omega_m}\right)-j\,4\sin\left(\frac{\pi\omega}{\omega_m}\right)+j\,14\sin\left(\frac{2\pi\omega}{\omega_m}\right)}, \\ \mathscr{S}_{31}(\omega) = \dfrac{4\left[2\cos\left(\frac{3\pi\omega}{2\omega_m}\right)-3j\,\sin\left(\frac{\pi\omega}{2\omega_m}\right)+j\,\sin\left(\frac{3\pi\omega}{2\omega_m}\right)\right]}{1-2\cos\left(\frac{\pi\omega}{\omega_m}\right)+13\cos\left(\frac{2\pi\omega}{\omega_m}\right)-j\,4\sin\left(\frac{\pi\omega}{\omega_m}\right)+j\,14\sin\left(\frac{2\pi\omega}{\omega_m}\right)}. \end{cases} \tag{C14}$$

We execute similar analyses at port 2 and port 3 and get the scattering parameters

$$\begin{cases} \mathscr{S}_{12}(\omega) = \dfrac{4\left[-1+3\cos\left(\frac{\pi\omega}{\omega_m}\right)+2j\,\sin\left(\frac{\pi\omega}{\omega_m}\right)\right]}{1-2\cos\left(\frac{\pi\omega}{\omega_m}\right)+13\cos\left(\frac{2\pi\omega}{\omega_m}\right)-j\,4\sin\left(\frac{\pi\omega}{\omega_m}\right)+j\,14\sin\left(\frac{2\pi\omega}{\omega_m}\right)}, \\ \mathscr{S}_{22}(\omega) = \dfrac{1-2\cos\left(\frac{\pi\omega}{\omega_m}\right)-3\cos\left(\frac{2\pi\omega}{\omega_m}\right)-j\,6\sin\left(\frac{2\pi\omega}{\omega_m}\right)}{1-2\cos\left(\frac{\pi\omega}{\omega_m}\right)+13\cos\left(\frac{2\pi\omega}{\omega_m}\right)-j\,4\sin\left(\frac{\pi\omega}{\omega_m}\right)+j\,14\sin\left(\frac{2\pi\omega}{\omega_m}\right)}, \\ \mathscr{S}_{32}(\omega) = \dfrac{4\left[2\cos\left(\frac{3\pi\omega}{2\omega_m}\right)+j\,\sin\left(\frac{\pi\omega}{2\omega_m}\right)+j\,\sin\left(\frac{3\pi\omega}{2\omega_m}\right)\right]}{1-2\cos\left(\frac{\pi\omega}{\omega_m}\right)+13\cos\left(\frac{2\pi\omega}{\omega_m}\right)-j\,4\sin\left(\frac{\pi\omega}{\omega_m}\right)+j\,14\sin\left(\frac{2\pi\omega}{\omega_m}\right)}. \end{cases} \tag{C15}$$

and

$$\begin{cases} \mathscr{S}_{13}(\omega) = \dfrac{4\left[2\cos\left(\frac{3\pi\omega}{2\omega_m}\right)+j\,\sin\left(\frac{\pi\omega}{2\omega_m}\right)+j\,\sin\left(\frac{3\pi\omega}{2\omega_m}\right)\right]}{1-2\cos\left(\frac{\pi\omega}{\omega_m}\right)+13\cos\left(\frac{2\pi\omega}{\omega_m}\right)-j\,4\sin\left(\frac{\pi\omega}{\omega_m}\right)+j\,14\sin\left(\frac{2\pi\omega}{\omega_m}\right)}, \\ \mathscr{S}_{23}(\omega) = \dfrac{4\left[2\cos\left(\frac{3\pi\omega}{2\omega_m}\right)-3j\,\sin\left(\frac{\pi\omega}{2\omega_m}\right)+j\,\sin\left(\frac{3\pi\omega}{2\omega_m}\right)\right]}{1-2\cos\left(\frac{\pi\omega}{\omega_m}\right)+13\cos\left(\frac{2\pi\omega}{\omega_m}\right)-j\,4\sin\left(\frac{\pi\omega}{\omega_m}\right)+j\,14\sin\left(\frac{2\pi\omega}{\omega_m}\right)}, \\ \mathscr{S}_{33}(\omega) = \dfrac{1-2\cos\left(\frac{\pi\omega}{\omega_m}\right)-3\cos\left(\frac{2\pi\omega}{\omega_m}\right)-j\,4\sin\left(\frac{\pi\omega}{\omega_m}\right)-j\,6\sin\left(\frac{2\pi\omega}{\omega_m}\right)}{1-2\cos\left(\frac{\pi\omega}{\omega_m}\right)+13\cos\left(\frac{2\pi\omega}{\omega_m}\right)-j\,4\sin\left(\frac{\pi\omega}{\omega_m}\right)+j\,14\sin\left(\frac{2\pi\omega}{\omega_m}\right)}. \end{cases} \tag{C16}$$

Equations (C14)–(C16) are the major results of this section. They transform into Eq. (37) at operational frequency $\omega = (2k+1)\omega_m, k = 0,\ 1,\ 2,\ 3\ldots$.

3. Ultrabroad-band circulator

With timing error, the Fourier series at three ports can be expressed as

$$V_1^-(t) = 0, \tag{C17}$$

$$V_2^-(t) = \sum_{n\neq 0} \frac{j\cos\frac{n\pi}{2}[1-\exp(-jn\omega_m|\Delta\tau|)]}{n\pi} e^{j(\omega+n\omega_m)t} \times e^{-j\omega\frac{T_m}{4}} + \left(1-\frac{2|\Delta\tau|}{T_m}\right) e^{-j\omega\frac{T_m}{4}} e^{j\omega t}, \tag{C18}$$

$$V_3^-(t) = \sum_{n\neq 0} \frac{-j[1+(-1)^n][1-\exp(-jn\omega_m|\Delta\tau|)]}{2n\pi} \times e^{j(\omega+n\omega_m)t} e^{-j\omega\frac{T_m}{2}} + \frac{2|\Delta\tau|}{T_m} e^{-j\omega\frac{T_m}{2}} e^{j\omega t}. \tag{C19}$$

The above equation indicates that the ultrabroad-band circulator has the same IM products compared with the ultrabroad-band isolator.

[1] L. Onsager, Reciprocal relations in irreversible processes. I., Phys. Rev. **7**, 405 (1931).

[2] L. Onsager, Reciprocal relations in irreversible processes. II., Phys. Rev. **38**, 2265 (1931).

[3] H. B. G. Casimir, Reciprocity theorems and irreversible processes, Proc. IEEE **51**, 1570 (1963).

[4] C. Caloz, A. Alù, S. Tretyakov, D. Sounas, K. Achouri, and Z.-L. D. Leger, Electromagnetic Nonreciprocity, Phys. Rev. Appl. **10**, 047001 (2018).

[5] D. M. Pozar, *Microwave Engineering* (Wiley, New York, 2011).

[6] Z. Yu and S. Fan, Complete optical isolation created by indirect interband photonic transitions, Nat. Photonics **3**, 91 (2009).

[7] H. Lira, Z. Yu, S. Fan, and M. Lipson, Electrically Driven Nonreciprocity Induced by Interband Photonic Transition on a Silicon Chip, Phys. Rev. Lett. **109**, 033901 (2012).

[8] K. Fang, Z. Yu, and S. Fan, Photonic Aharonov-Bohm Effect Based on Dynamic Modulation, Phys. Rev. Lett. **108**, 153901 (2012).

[9] D. L. Sounas, C. Caloz, and A. Alù, Giant non-reciprocity at the subwavelength scale using angular momentum-biased metamaterials, Nat. Commun. **4**, 2407 (2013).

[10] S. Qin, Q. Xu, and Y. E. Wang, Nonreciprocal components with distributedly modulated capacitors, IEEE Trans. Microw. Theory Techn. **62**, 2260 (2014).

[11] N. A. Estep, D. L. Sounas, J. Soric, and A. Alù, Magnetic-free non-reciprocity and isolation based on parametrically modulated coupled-resonator loops, Nat. Phys. **10**, 923 (2014).

[12] R. Fleury, D. L. Sounas, C. F. Sieck, M. R. Haberman, and A. Alù, Sound isolation and giant linear nonreciprocity in a compact acoustic circulator, Science **343**, 516 (2014).

[13] N. Reiskarimian and H. Krishnaswamy, Magnetic-free non-reciprocity based on staggered commutation, Nat. Commun. **7**, 11217 (2016).

[14] D. L. Sounas and A. Alù, Non-reciprocal photonics based on time modulation, Nat. Photonics **11**, 774 (2017).

[15] T. Dinc, M. Tymchenko, A. Nagulu, D. Sounas, A. Alù, and H. Krishnaswamy, Synchronized conductivity modulation to realize broadband lossless magnetic-free non-reciprocity, Nat. Commun. **8**, 795 (2017).

[16] L. Bi, J. Hu, P. Jiang, D. H. Kim, G. F. Dionne, L. C. Kimerling, and C. A. Ross, On-chip optical isolation in monolithically integrated non-reciprocal optical resonators, Nat. Photonics **5**, 758 (2011).

[17] L. Fan, J. Wang, L. T. Varghese, H. Shen, B. Niu, Y. Xuan, A. M. Weiner, and M. Qi, An all-silicon passive optical diode, Science **335**, 447 (2012).

[18] B. J. Chapman, *et al.*, Widely tunable on-chip microwave circulator for superconducting quantum circuits, Phys. Rev. X **7**, 041043 (2017).

[19] A. Kord, D. L. Sounas, and A. Alù, Magnet-less circulators based on spatiotemporal modulation of bandstop filters in a delta topology, IEEE Trans. Microw. Theory Techn. **66**, 911 (2018).

[20] T. Dinc, A. Nagulu, and H. Krishnaswamy, A millimeter-wave non-magnetic passive SOI CMOS circulator based on spatio-temporal conductivity modulation, IEEE J. Solid-State Circuits **52**, 3276 (2017).

[21] N. Reiskarimian, A. Nagulu, T. Dinc, and H. Krishnaswamy, Nonreciprocal electronic devices: A hypothesis turned into reality, IEEE Microw. Mag. **20**, 94 (2019).

[22] M. Duarte, C. Dick, and A. Sabharwal, Experiment-driven characterization of full-duplex wireless systems, IEEE Trans. Wirel. Commun. **11**, 4296 (2012).

[23] A. Kord, D. L. Sounas, Z. Xiao, and A. Alù, Broadband cyclic-symmetric magnetless circulators and theoretical bounds on their bandwidth, IEEE Trans. Microw. Theory Techn. **66**, 5472 (2018).

[24] J. Zhou, *et al.*, Integrated full duplex radios, IEEE Commun. Mag. **55**, 142 (2017).

[25] Y. Yu, G. Michetti, A. Kord, M. Pirro, D. Sounas, Z. Xiao, C. Cassella, A. Alù, and M. Rinaldi, Highly-linear magnetfreee microelectromechanical circulators, IEEE J. Microelectromech. Syst. **28**, 933 (2019).

[26] Y. Yu, G. Michetti, M. Pirro, A. Kord, D. Sounas, Z. Xiao, C. Cassella, A. Alù, and M. Rinaldi, Radio frequency magnetfree circulators based on spatialtemporal modulation of surface acoustic wave filters, IEEE Trans. Microw. Theory Techn. **67**, 4773 (2019).

[27] D. L. Sounas, J. Soric, and A. Alù, Broadband passive isolators based on coupled nonlinear resonances, Nat. Electron. **1**, 113 (2018).

[28] Y. Shi, Z. Yu, and S. Fan, Limitations of nonlinear optical isolators due to dynamic reciprocity, Nat. Photonics **9**, 388 (2015).

[29] D. L. Sounas and A. Alù, Fundamental bounds on the operation of Fano nonlinear isolators, Phys. Rev. B **97**, 115431 (2018).

[30] K. Fang, Z. Yu, and S. Fan, Realizing effective magnetic field for photons by controlling the phase of dynamic modulation, Nat. Photonics **6**, 782 (2012).

[31] A. Kord, D. L. Sounas, and A. Alù, Low-loss broadband magnetless circulators for full-duplex radios, *Proc. IEEE MTT-S Int. Microw. Symp*, Philadelphia, Pennsylvania, USA, June 2018.

[32] A. Nagulu and H. Krishnaswamy, Non-magnetic CMOS switched-transmission-line circulators with high power handing and antenna balancing: Theory and implementation, IEEE J. Solid-State Circuits **54**, 1288 (2019).

[33] A. Nagulu and H. Krishnaswamy, in *IEEE International Solid-State Circuits Conference-(ISSCC)* (2019), pp. 446–448.

[34] A. Nagulu, T. Dinc, Z. Xiao, M. Tymchenko, D. Sounas, A. Alù, and H. Krishnaswamy, Nonreciprocal components based on switched transmission lines, IEEE Trans. Microw. Theory Techn. **66**, 4706 (2018).

[35] B. D. H. Tellegen, The gyrator, a new electric network element, Philips Res. Rept. **3**, 81 (1948).

[36] K. M. Adams, E. F. A. Deprettere, and J. O. Voorman, The gyrator in electronic systems, Adv. Electron. Electron Phys. **37**, 79 (1975).

[37] M. Tymchenko, D. Sounas, and A. Alù, in *IEEE International Symposium on Antennas and Propagation and USNC/URSI National Radio Science Meeting* (2017).

[38] A. Kord, D. Sounas, and A. Alù, Pseudo-linear time-invariant magnetless circulators based on differential spatiotemporal modulation of resonant junctions, IEEE Trans. Microw. Theory Techn. **66**, 2731 (2018).

[39] D. Sounas, N. A. Estep, A. Kord, and A. Alù, Angular-momentum biased circulators and their power consumption, IEEE Antenn. Wirel. Propag. Lett. **17**, 1963 (2018).